Mechanoaccumulation of non-muscle myosin IIB during mitosis requires its translocation activity

Chao Wang[1,2,*], Jingjing Ding[1,2,*], Qiaodong Wei[3], Shoukang Du[1,2], Xiaobo Gong[3], Ting Gang Chew[1,2,#]

Affiliations

[1]Department of Orthopedics of the Second Affiliated Hospital, Zhejiang University School of Medicine, Zhejiang University, Hangzhou 310058, China

[2]The Zhejiang University-University of Edinburgh Institute, Zhejiang University School of Medicine, Zhejiang University, Hangzhou 310058, China

[3]Department of Engineering Mechanics, School of Naval Architecture, Ocean and Civil Engineering, Shanghai Jiao Tong University, Shanghai 200240, China

*Co-first authors

#Correspondence to: Ting Gang Chew (tinggchew@intl.zju.edu.cn)

Running title: NMIIB mechanoresponse require its motor activity

Abstract

Non-muscle myosin II (NMII) is a force-generating mechanosensitive enzyme that responds to mechanical forces exerted on cells. Mechanoresponse of NMIIs confers mechanical adaptability to cells growing and dividing in a physically complex microenvironment. In response to mechanical forces, NMIIs mechanoaccumulate at the cell cortex with applied stress. Much less is known about how NMII mechanoaccumulation is mechanistically regulated. In this study, we subject cells in mitosis to compressive forces and show that mitotic cells promote active RhoA mechanoaccumulation, and via ROCK signaling, activate and stabilize NMIIB at the cell cortex. In line with RhoA in activating the myosin motor activity, we further show that the motor activity driving actin filament translocation, but not just the actin-binding function of NMIIB plays a dominant regulatory role in NMIIB mechanoaccumulation. Thus, the motor activity coordinates structural movement and nucleotide state changes to fine-tune actin-binding affinity optimal for NMIIs to generate and respond to forces.

Introduction

Non-muscle myosin IIs (NMIIs) are a family of actin-based molecular motors that function with actin filaments to generate forces to drive cell morphogenesis, cell migration and cell division (Murrell et al., 2015; Vicente-Manzanares et al., 2009). NMIIs and actin filaments form a layer of contractile cytoskeletal network at the cell cortex underlying the cell membrane to drive changes of cell shape (Kelkar et al., 2020). One key role of NMII's contractility is to promote mitotic cell rounding in cells transiting from interphase into mitosis, and to sustain a round cell shape throughout mitosis (Nishimura et al., 2019; Ramanathan et al., 2015; Ramkumar and Baum, 2016). Cells that are not able to maintain a round cell shape when dividing in a physically confined environment have defects in their mitotic spindle stability and form multipolar spindles that lead to chromosome mis-segregation and aneuploidy (Cadart et al., 2014; Lancaster et al., 2013; Matthews et al., 2020).

As cells enter mitosis, activation of cyclin-dependent kinase 1 (CDK1) triggers the cytoplasmic shuttling of a Rho guanine nucleotide exchange factor (RhoGEF) Ect2 to activate RhoA, which in turn binds to the cell membrane and recruits its effectors such as anillin, formin and Rho-associated kinase (ROCK) to activate NMII sliding on actin filaments homeostatically maintained at the cell cortex (Chew et al., 2017; Maddox and Burridge, 2003; Matthews et al., 2012; Ramanathan et al., 2015; Rosa et al., 2015). Activation of this signaling cascade results in generation of higher cell surface tension, which leads to mitotic cell rounding crucial in providing an ideal cell geometry to undergo mitosis and cytokinesis (Cattin et al., 2015; Lancaster et al., 2013; Stewart et al., 2011).

NMII consists of two heavy chains, two regulatory light chains (MRLC) and two essential light chains (ELC). The myosin heavy chain has a globular head, a flexible neck structure and an elongated tail region (Sweeney and Houdusse, 2010). NMII is activated when the neck structure is bound by MRLC phosphorylated via RhoA-mediated ROCK signaling (Amano et al., 1996; Garrido-Casado et al., 2021). Further phosphoregulation of the myosin tail region assembles active NMIIs into multimeric myofilaments that have high affinity to actin filaments (Garrido-Casado et al., 2021; Juanes-Garcia et al., 2015). The motor activity in the globular head of myofilaments catalyses nucleotide hydrolysis to form the cross-bridge and to translocate actin filaments via lever arm movement (Sweeney and Houdusse, 2010). Apart from force generation, NMIIs sense and respond to mechanical inputs in cells. In response to mechanical forces, NMIIs accumulate at the cell cortex of the stressed region in cells (Luo et al., 2013). The three mammalian NMII paralogs (NMIIA, NMIIB, NMIIC) accumulate at the region that is mechanically stressed (mechanoaccumulation), with NMIIB showing differential mechanoresponse across cell types and cell cycle phases (Schiffhauer et al., 2016). Mechanoaccumulation of NMIIs is influenced by the length of its neck structure in which an extended length of the neck structure facilitates its accumulation (Luo et al., 2013). Furthermore, phosphoregulation of NMII's tail region that modulates myofilament assembly states contributes to the ability of NMIIs to accumulate at the cell cortex in response to mechanical stress (Schiffhauer et al., 2019).

72 Much has been done to understand the force generation mechanism of NMIIs, less is known about
73 how NMII's mechanoresponse is regulated. In this study, we aimed to understand the mechanism
74 for NMIIB mechanoaccumulation in mitotic cells responding to compressive forces. By using a cell
75 contractility reporter cell line, we found that cells respond to compressive stress during mitosis by
76 accumulating active RhoA at the cell cortex, which in turn leads to higher activation and
77 mechanoaccumulation of NMIIB. Interestingly, further genetic dissection of NMIIB head domain by
78 using mutations that uncouple actin-binding function and motor activity to translocate actin
79 filaments showed that the translocation activity of NMIIB plays a primary role for its ability to
80 undergo mechanoaccumulation. We propose that the NMIIB translocation activity coordinates
81 structural changes to nucleotide state changes to prepare NMIIBs of differential actin-binding
82 affinity, so to achieve mechanoaccumulation at the cell cortex in response to compressive forces
83 during mitosis.

84

85 **Results**

86 **Construction and validation of a cell contractility reporter cell line**

87 To study how NMII mechanoresponse is regulated during mitosis, we made a human MCF10A
88 mammary epithelial cell stably expressing fluorescently tagged non-muscle myosin IIB (mEmerald-
89 NMIIB) and active RhoA reporter consisting of the RhoA-binding domain of anillin (mRuby2-AHPH)
90 (Acharya et al., 2018; Beaudet et al., 2020; Cavanaugh et al., 2022; Piekny and Glotzer, 2008;
91 Priya et al., 2015). NMIIB localizes to the cell cortex in the early mitosis and functions downstream
92 of active RhoA to generate cortical tension (Maddox and Burridge, 2003; Taneja et al., 2020). Live-
93 cell microscopy imaging revealed that NMIIB and active RhoA localized to the cell cortex starting
94 from early mitosis and enriched at the division site during mitosis and cytokinesis, consistent with
95 previous studies and their roles in tension generation at the cell cortex during cell division (Fig. 1 A)
96 (Maddox and Burridge, 2003; Piekny and Glotzer, 2008; Taneja et al., 2020). To examine the
97 activity of mEmerald-NMIIB, we treated mitotic cells with low, medium and high concentrations of
98 the low cytotoxic and photostable NMII inhibitor para-nitro-blebbistatin (p-nitroblebb), which lowers
99 the actin affinity of NMII heads (Kepiro et al., 2014; Rauscher et al., 2018). Mitotic cells treated with

100 a low concentration of p-nitroblebb showed punctate cortical NMIIB patterns (Fig. 1 B, insets).
101 Higher concentrations of p-nitroblebb resulted in a decreasing NMIIB intensity at the mitotic cell
102 cortex (Figs. 1 B and C). Analyses of the NMIIB turnover at the mitotic cell cortex with the
103 fluorescence recovery after photobleaching technique (FRAP) showed an increase of the immobile
104 fractions of NMIIB upon increased concentrations of p-nitroblebb (Figs.1 D and E; DMSO: 0.27 ±
105 0.08; [Low]: 0.45 ± 0.01; [Medium]: 0.50 ± 0.01; [High]: 0.59 ± 0.03). The recovery half time of
106 cortical NMIIB decreased when increasing concentrations of p-nitroblebb were used (Fig. 1 E;
107 DMSO: 20.33 ± 2.09 s; [Low]: 12.61 ± 1.46 s; [Medium]: 11.30 ± 0.59 s; [High]: 9.49 ± 0.05 s). The
108 FRAP analysis suggested that a decrease of NMIIB recovery half time with higher immobile
109 fractions characterizes inhibition of mEmerald-NMIIB function at the cell cortex by the NMII inhibitor.

110

111 To test the response of active RhoA reporter, mitotic cells were treated with a RhoA inhibitor C3
112 exoenzyme that prevents activation of RhoA, both active RhoA and NMIIB disappeared from the
113 mitotic cell cortex (Fig. 1 F). This indicates that mRuby2-AHPH reliably reports the active state of
114 RhoA. Taken together, AHPH-mRuby2 and mEmerald-NMIIB report the status of cellular
115 contractility during mitosis and cytokinesis.

116

117 **Mechanoaccumulation of NMIIB and active RhoA at the mitotic cell cortex**

118 To study how NMIIB responds to mechanical forces during mitosis, we compressed the mitotic
119 cells with a soft elastic gel and a weight (Fig. 2 A). When compressive forces were exerted on the
120 mitotic cells, the cell has enlarged its diameter, and the cell height has decreased from 22.89 ±
121 1.88 μm to 15.19 ± 1.19 μm (Figs. 2 B and C). Within 2 minutes after compression, we observed
122 increased intensity of NMIIB at the mitotic cell cortex. In average, there was 1.45 ± 0.29-fold
123 increase of cortical NMIIB intensity in individual cells (Fig. 2 D). Concomitantly, active RhoA
124 increased its intensity at the mitotic cell cortex by 1.54 ± 0.31-fold compared to that of before
125 compression (Figs. 2 E and F). Approximately 76.5% individual cells showed an increase of both
126 active RhoA and NMIIB at the mitotic cell cortex after compression (Fig. S1 A), suggesting that in

127 response to compressive forces, mitotic cells accumulate more active RhoA leading to an
128 accumulation of NMIIB at the cell cortex. Consistently, individual mitotic cells expressing active
129 RhoA reporter using Rhotekin Rho binding domain (Mahlandt et al., 2021) also showed
130 mechanoaccumulation of active RhoA at the cell cortex in response to compressive forces (Fig. S1
131 B). Furthermore, compressive forces have resulted in more activated NMII as revealed by higher
132 level of phosphorylated myosin regulatory light chain (p-MRLC) in the cell lysate from compressed
133 cells (Fig S1 C).

134

135 To test whether mechanoaccumulation of active RhoA at the cell cortex depends on cell surface
136 tension, we decreased cell surface tension by inhibiting NMII function with p-nitroblebb treatment.
137 We first measured cell surface tension in mitotic cells treated with p-nitroblebb using the
138 micropipette aspiration technique. The mitotic cell surface tension decreased to 56%, 44%, 31% of
139 the control group after treatments with low, medium and high concentrations of p-nitroblebb,
140 respectively (Fig. S1 D; DMSO: 894.90 ± 186.74 pN/μm; [Low]: 500.42 ± 90.64 pN/μm; [Medium]:
141 393.87 ± 121.08 pN/μm; [High]: 281.58 ± 60.84 pN/μm). Upon p-nitroblebb treatment, we observed
142 that the cortical localization of active RhoA decreased when cell surface tension has been lowered
143 for 3-fold in mitotic cells treated with p-nitroblebb, suggesting that RhoA could respond to the
144 cortical tension generated by NMII during mitosis (Fig. S1 E).

145

146 Next, we used FRAP to analyze the cortical NMIIB turnover in mitotic cells under compression. We
147 found that compression in mitotic cells has slowed down the turnover of the cortical NMIIB, with an
148 increase of the recovery half time of 27.75 ± 0.86 s as compared to that of in the uncompressed
149 mitotic cells that was 18.85 ± 1.79 s (Figs. 2 G and H). Thus, compressive forces stabilize NMIIB at
150 the mitotic cell cortex leading to mechanoaccumulation of NMIIB in a RhoA-dependent manner.

151

152

153 **Roles of RhoA/ROCK and CDK1 in mitotic NMIIB mechanoaccumulation under compression**

154 When cells are entering mitosis from G2 phase, cyclin-dependent kinase 1 (CDK1) regulates
155 RhoGEF Ect2 to activate RhoA, which in turn exerts its effects on the actomyosin network through
156 ROCK signaling (Fig. 3 A) (Matthews et al., 2012; Rosa et al., 2015). Since we found that active
157 RhoA responds to compressive forces during mitosis and leads to NMIIB activation and
158 accumulation at the cell cortex, we asked whether CDK1 and ROCK are involved in the
159 mechanoaccumulation of RhoA and NMIIB during mitosis. We first examined the effects of CDK1
160 and ROCK inhibition in mitotic cells not subjected to compressive forces. When mitotic cells were
161 chemically inhibited by the ROCK inhibitor Y-27632, NMIIB decreased about 2-fold at the cell
162 cortex while active RhoA did not show significant changes, which is consistent with NMIIB
163 functions downstream of ROCK following RhoA activation (Figs. S2 A and B). Consistently, there
164 was about 20% decrease of cell surface tension from 965.34 ± 133.34 pN/μm in the control group
165 to 770.04 ± 160.08 pN/μm in the Y-27632 treated group (Fig. S2 C). Of note, a decrease of cell
166 surface tension by the concentration of Y-27632 used in this study was not sufficient to reduce
167 active RhoA from the cell cortex. When we treated mitotic cells with CDK1 inhibitor RO-3306,
168 NMIIB decreased about 2-fold at the cell cortex and the cell surface tension decreased 15% to
169 821.67 ± 106.14 pN/μm compared to the control group (Figs. S2 B and C). Interestingly, active
170 RhoA showed an increased accumulation at the cell cortex upon inhibition of CDK1 (Fig. S2 B).
171 Thus, CDK1 appears to regulate NMIIB independent of RhoA activation in mitotic cells, which is
172 different from that of in interphase cells entering mitosis.

173

174 Next, we examined the mechanoresponse of NMIIB and active RhoA in mitotic cells treated with
175 ROCK or CDK1 inhibitors (Fig. S2 D). When mitotic cells were compressed for about 8 minutes in
176 the presence of Y-27632, there was a decrease of cortical NMIIB as compared to the control group
177 that showed an increase of cortical NMIIB after compression (Figs. 3 A, B and C). Active RhoA
178 accumulated at the mitotic cell cortex after compression in the presence or absence of Y-27632
179 (Figs. 3 A and B and C). Similarly, when mitotic cells were compressed in the presence of RO-
180 3306, NMIIB decreased its intensity at the cell cortex while active RhoA showed

181 mechanoaccumulation at the cell cortex (Figs. A D and E). Collectively, our data show that ROCK
182 and CDK1 are required for NMIIB to accumulate at the cell cortex in response to compressive
183 forces during mitosis, however, CDK1 appears to exert its effect on NMIIB independent of active
184 RhoA.

185

186 **Phosphoregulation of NMIIB tail region is not involved in NMIIB mechanoaccumulation**

187 RhoA / ROCK signaling modulates NMII through phosphorylation of MRLC that associates with
188 NMII's head domain. In addition, NMII is also regulated by the phosphorylation of its tail region,
189 which is involved in regulating myosin II filament assembly (Heissler and Sellers, 2016).
190 Phosphorylation of NMIIB S1935 lowers the ability of NMIIB to assemble into myofilaments (Fig. 4
191 A) (Juanes-Garcia et al., 2015; Schiffhauer et al., 2019). To study the role of NMIIB tail
192 phosphorylation, we first generated three cell lines stably expressing wild type NMIIB, NMIIB
193 containing a non-phosphorylatable alanine residue at S1935 (S1935A), and NMIIB containing a
194 phosphomimetic aspartate residue at S1935 (S1935D), respectively. The endogenous NMIIB in
195 these cell lines was depleted using CRISPR interference (CRISPRi) that switches off gene
196 expression from its promoter and does not interfere with the transgene expression (Fig. S3 A and
197 B). Cells expressing NMIIB S1935D showed a decrease in the cytoskeletal fraction compared to
198 cells expressing wild type NMIIB or NMIIB S1935A, indicating less cytoskeletal-bound NMIIB
199 myofilaments were present (Fig. 4 B and C).

200

201 When we examined the NMIIB tail phosphomutants, we found that mitotic cells expressing NMIIB
202 S1935D generated lower cell surface tension (1007.94 ± 130.21 pN/μm in wild type NMIIB and
203 677.67 ± 111.03 pN/μm in NMIIB S1935D) but were able to demonstrate mechanoaccumulation of
204 NMIIB S1935D after compression (Figs. 4 D and E; S3 C). Mitotic cells expressing NMIIB S1935A
205 exhibited a similar level of cell surface tension (1069.76 ± 158.13 pN/μm in NMIIB S1935A) and
206 mechanoaccumulation as in cells expressing wild type NMIIB (Figs. 4 D and E; S3 C). Thus,
207 phosphorylation of NMIIB S1935 at the tail domain affected NMIIB's function in cell surface tension

208 generation but less on the mechanoresponse of NMIIB, in line with the previous study showing that
209 the NMIIB tail domain fine-tuned the NMIIB mechanosensitive dynamics and the phosphomutants
210 could accumulate with varying degree at the cell cortex in epithelial cells in response to mechanical
211 stress (Schiffhauer et al., 2019).

212

213 **NMIIB translocation activity is required for its mechanoaccumulation under compression**

214 Our results showed that regulation of NMII's head domain is important for NMIIB to accumulate at
215 the cell cortex in response to compressive forces during mitosis. NMII's head domain has two
216 properties namely actin-binding functions and motor activity to translocate actin filaments
217 (Sweeney and Houdusse, 2010). Previous studies showed that NMII's mutations that selectively
218 uncouple these two properties have revealed distinct contributions of each property to NMII's
219 cellular functions (Choi et al., 2008; Ma et al., 2012; Smutny et al., 2010). To see the roles of these
220 properties in regulating NMIIB mechanoaccumulation, we expressed two previously characterised
221 NMIIB mutants NMIIB R709C or NMIIB R241A that are defective in motor activity but retaining their
222 ability to bind actin filaments (Kim et al., 2005; Osorio et al., 2019), and one NMIIB mutant K647A
223 that has a weakening actin-binding function (von der Ecken et al., 2016) in the reporter cells (Fig. 5
224 A). We further depleted the endogenous NMIIB in these cell lines using CRISPRi.

225

226 Cytoskeletal fractionation analyses showed that cells expressing NMIIB R709C or R241A have an
227 increased NMIIB cytoskeletal fraction than cells expressing wild type NMIIB or NMIIB S1935D,
228 indicating a strong cytoskeletal binding of these two NMIIB mutant proteins despite a defective
229 motor activity (Figs. 5 B and C, right panels). Interestingly, when we compressed the mitotic cells
230 expressing NMIIB R709C or R241A, there was no significant increase of cortical NMIIB intensity
231 compared to that of in control cells expressing wild type NMIIB (Figs. 5 B and C, left and middle
232 panels). In contrast, compression of mitotic cells expressing NMIIB K647A, which has more NMIIB
233 mutant proteins in the soluble fraction, showed a similar mechanoaccumulation of NMIIB at the cell
234 cortex as in control cells. Thus, our data show that the translocation activity of NMIIB, but not just

235 the actin-binding function of the NMIIB's head domain, is required for NMIIB to accumulate at the
236 cell cortex in response to compressive forces during mitosis.

237

238 **NMIIB translocation activity has a dominant role in regulating its mechanoaccumulation**

239 Next, we asked whether the NMIIB tail mutation S1935D could reduce the tight cytoskeletal
240 association of the NMIIB translocation mutants and hence reverting NMIIB mechanoresponse. To
241 this end, we constructed three NMIIB mutants containing double mutations R709C S1935D,
242 R241A S1935D and K647A S1935D, respectively. We first determined the proportion of the
243 cytoskeletal fraction in protein lysates extracted from these NMIIB double mutants. The results
244 showed that cells expressing NMIIB R709C S1935D and NMIIB R241A S1935D have more
245 insoluble cytoskeletal-bound NMIIB mutant proteins compared to control cells (Fig. 6 A).
246 Compression of these two NMIIB mutant cells showed no significant increase of the cortical NMIIB
247 at the cell cortex compared to cells expressing wild type NMIIB or NMIIB S1935D (Figs. 6 B and C).
248 Cells expressing NMIIB K647A S1945D, have more mutant proteins in the soluble fraction
249 compared to control cells and retain the ability to accumulate the cortical NMIIB double mutant
250 protein at the cell cortex in response to compression (Figs. 6 A B and C). Our data show that
251 NMIIB S1935D mutation does not revert mechanoaccumulation defects of NMIIB translocation
252 mutants, and the NMIIB translocation activity at its head domain plays a dominating role in
253 regulating NMIIB mechanoaccumulation at the cell cortex during mitosis.

254

255 **Discussion**

256 NMIIs accumulate at the subcellular region with applied mechanical stresses (Luo et al., 2013).
257 Mechanoresponse of NMIIs facilitates cellular mechanosensing during cell migration and cell
258 division and confers mechanical adaptation to cancer cells living in physically challenging
259 microenvironment (Nguyen et al., 2022). Within a tissue environment, cells constantly experience
260 mechanical stresses such as compressive stress from surrounding cells and the extracellular
261 matrix. This is particularly significant in an overgrowth tumor environment where solid stress or

262 compressive stress accumulates inside the tumors (Nia et al., 2020). Normal or cancer cells that
263 are not able to mechanically adapt to the constantly changing microenvironment by engaging
264 mechanoresponse accumulate cell division defects that lead to aneuploidy (Cattin et al., 2015;
265 Matthews et al., 2020).

266

267 During the cross-bridge cycle of force generation, NMII binds and slides actin filaments (Sweeney
268 and Houdusse, 2010). Interestingly, these two closely related biophysical properties can be
269 genetically uncoupled in different cellular functions of NMIIs. Previous studies showed that
270 maturation of nascent adhesions in migrating cells and division of certain cell types require NMIIs
271 to bind and crosslink actin networks but does not involve its motor activity (Choi et al., 2008; Ma et
272 al., 2012). In contrast, NMIIs bind and slide actin filaments during cell-cell adhesions and
273 embryonic cell division (Kasza et al., 2019; Osorio et al., 2019; Smutny et al., 2010). We tested this
274 differential requirement of NMII in its mechanoresponse during mitosis. Using two NMIIB
275 mutations (R709C and R241A in NMIIB) that are motor dead but retaining actin-binding function
276 (Ma et al., 2012; Osorio et al., 2019), we revealed that mechanoaccumulation of NMIIB at the
277 mitotic cell cortex requires the translocation activity of NMIIB. Interestingly, a mutation in loop 2 of
278 the actin-binding surface of NMIIB (K647A in NMIIB), which regulates the cleft closure of U50 and
279 L50 subdomains of NMIIs for strong actin-binding function (Onishi et al., 2006; von der Ecken et al.,
280 2016), does not dampen NMIIB mechanoresponse. Thus, actin-binding function of NMIIs alone is
281 not sufficient to regulate mechanoaccumulation of NMIIB at the mitotic cell cortex, and
282 counterintuitively, the motor activity of NMIIB in driving actin filament translocation is essential in
283 NMIIB mechanoresponse.

284

285 Activation of RhoA/ROCK signaling pathway leads to MRLC phosphorylation and is associated
286 with an increase of the actin-activated ATPase kinetics of myosin head domain and hence its
287 motor activity (Amano et al., 1996; Heissler and Sellers, 2016; Nayak et al., 2020). We found that
288 mechanoaccumulation of NMIIB is a result of active RhoA mechanoaccumulation at the mitotic cell
289 cortex. Through the effector ROCK, mechanoaccumulation of active RhoA drives higher activation

290 of myosin motor domain and stabilization of NMIIB at the cell cortex in response to compressive
291 forces in mitotic cells. Interestingly, NMIIB mechanoaccumulation at the cell cortex can be
292 independent of active RhoA accumulation as CDK1 inhibition leads to decreased cortical NMIIB
293 but higher cortical active RhoA in compressed mitotic cells. Similar observation has been identified
294 in starfish oocytes undergoing meiotic division in which RhoA is activated when CDK1 is inhibited
295 during surface contraction waves (Bischof et al., 2017). Thus, CDK1 regulates NMIIB
296 mechanoaccumulation during mitosis independent of active RhoA. This contrasts with CDK1's
297 function in activating Ect2/RhoA/ROCK signaling and NMIIs when cells enter mitosis from
298 interphase (Matthews et al., 2012; Rosa et al., 2015).

299

300 Mechanical activation of RhoA happens at the cell-cell adherens junctions and the cell-matrix focal
301 adhesion to reinforce actomyosin contractility in response to mechanical stress (Acharya et al.,
302 2018; Guilluy et al., 2011). Our study, to our knowledge, is the first to show accumulation of active
303 RhoA at the cell cortex in response to compressive forces during mitosis. Mechanoaccumulation of
304 active RhoA at the cell cortex during mitosis was not previously identified although inhibition of its
305 downstream effector ROCK led to a decreased mechanoresponse of NMII (Schiffhauer et al.,
306 2016). In our study, we employed widely used live-cell active RhoA reporters (Koh et al., 2021;
307 Mahlandt et al., 2021) and focused only on mitotic cells using a microscopy with confocality and
308 high temporal resolution. This has facilitated a sensitive detection of RhoA mechanoresponse at
309 the cell cortex when mitosis is mechanically challenged.

310

311 Our finding implies that NMII mechanoaccumulation involves lever arm movement generated by
312 the motor activity. Lever arm movement is coupled to nucleotide state changes during Pi release
313 and ADP release and generates NMIIs of different nucleotide states and actin-binding affinity
314 (Debold, 2021; Sweeney and Houdusse, 2010; Trivedi et al., 2015; Wulf et al., 2016). Consistently,
315 NMIIs engineered to have longer neck structure and hence larger lever arm movement have
316 stronger ability to mechanoaccumulate in cells (Luo et al., 2013). We propose a model that NMIIB
317 species of different actin-binding affinity are generated after lever arm movement and nucleotide

318 state changes. These NMIIB species bind actin filaments at varying affinity and in ensemble
319 display accumulation in response to compressive forces during mitosis. This notion is supported by
320 the existence of "Goldilocks zone" for the actin-binding affinity for an optimal
321 mechanoaccumulation as described for actin-binding proteins such as α-actinin, filamin and NMIIs
322 (Schiffhauer et al., 2016).

323

324 **Materials and methods**

325 **Cell lines and culture**

326 MCF10A cell lines were cultured in DMEM F-12 (Shanghai BasalMedia) with Glutamax (Gibco), 5%
327 horse serum (Biological Industries), 20 ng/ml EGF (Gibco), 0.5 mg/ml Hydrocortisone
328 (MedChemExpress), 100 ng/ml Cholera toxin (Sigma), 10 μg/ml Insulin (Biological Industries), 1%
329 Pen/Strep (Biological Industries) at 37°C with 5% CO2. The MCF10A cell line was a gift from Dr.
330 Kuan Yoow Chan from Zhejiang University. The cells were authenticated by Sangon Biotech and
331 were routinely checked for mycoplasma contamination in the lab using Myco-Blue Mycoplasma
332 Detector (Vazyme). MCF10A cells expressing mRuby2-AHPH and mEmerald-NMIIB, or dTomato-
333 2xrGBD were prepared by lentivirus transduction and were enriched using the fluorescence-
334 activated cell sorting (FACS). MCF10A cells expressing mEmerald-NMIIB WT, mEmerald-NMIIB
335 S1935A, and mEmerald-NMIIB S1935D, mEmerald-NMIIB R709C, mEmerald-NMIIB R241A,
336 mEmerald-NMIIB K647A, and all NMIIB double mutants, respectively, were prepared by lentivirus
337 transduction and selected with 2 μg/ml puromycin (Sangon Biotech) and were enriched using the
338 FACS. To knockdown the endogenous NMIIB, the lentivirus expressing pCRISPRi0003 containing
339 the guiding RNA (gRNA) targeting the NMIIB's 5' UTR region was transduced into the cells
340 expressing NMIIB mutants. Cells were selected with 6 μg/ml blasticidin (Solarbio) for 6 days and
341 were continued to grow without the antibiotic for another 1 to 3 days before the experiments.

342 **Drug treatments**

343 The following drugs were used in the study: NMII inhibitor: p-nitro-blebbistatin (Cayman Chemical,
344 24171); Rho inhibitor: C3 exoenzyme (Cytoskeleton, CT04); ROCK inhibitor: Y-27632

345 (MedChemExpress, HY-10583); CDK1 inhibitor: RO-3306 (Selleckchem, S7747). DMSO was used
346 to dissolve p-nitro-blebbistatin, Y-27632 and RO-3306. C3 exoenzyme was dissolved in water.
347 Details of concentrations used in the study are described in figure legends.

348 **Lentiviral expression constructs**

349 The following lentiviral transfer plasmids were used in the study: pTGL0427 containing mRuby2-
350 AHPH in which AHPH was subcloned from an Addgene plasmid #68026 (a gift from Michael
351 Glozter) and fused with mRuby2; pTGL0193 containing mEmerald-NMIIB, which was subcloned
352 from an Addgene plasmid #54192 (a gift from Michael Davidson); pTGL0594 containing dTomato-
353 2xrGBD subcloned from an Addgene plasmid #129625 (a gift from Dorus Gadella); pTGL0373
354 containing mEmerald-NMIIB S1935A; pTGL0374 containing mEmerald-NMIIB S1935D; pTGL0584
355 containing mEmerald-NMIIB R709C; pTGL0585 containing mEmerald-NMIIB R709C S1935D;
356 pTGL0582 containing mEmerald-NMIIB R241A; pTGL0583 containing mEmerald-NMIIB R241A
357 S1935D; pTGL0589 containing mEmerald-NMIIB K647A; pTGL0590 containing mEmerald-NMIIB
358 K647A S1935D; pTGL0386 containing KRAB and dCas9 for CRISPRi (a gift from Jorge Ferrer,
359 Addgene plasmid #118154); pCRISPRi0001 containing gRNA 5' GTGCTAAAGGAGCCCGGCGG
360 3' cloned into pTGL0386; pCRISPRi0002 containing gRNA 5' GCTGGATCTGTGGTCGCGGC 3'
361 cloned into pTGL0386; pCRISPRi0003 containing gRNA 5' GGACTGAGGCGCTGGATCTG 3'
362 cloned into pTGL0386. The 3rd generation lentiviral packaging system was used to prepare
363 lentiviral particles. In brief, packaging plasmids pRSV-Rev, pMDLg/pRRE, pMD2.G (gifts from
364 Didier Trono) were chemically transfected with the transfer plasmid into the 293Ta packaging cell
365 line (Genecopoeia, LT008) using GeneTwin transfection reagent (Biomed, TG101). After 3 days,
366 the culture medium was collected, filtered through a 0.45 μm filter, and then concentrated using the
367 lentivirus concentration solution (Genomeditech, GM-040801) before adding to MCF10A cells.

368 **Mitotic cell preparation**

369 To increase the mitotic cell number, cells cultured on the imaging chambered coverglass were
370 treated with 7.5 μM RO-3306 (Selleckchem) for 16 to 18 hours at 37 °C and were washed with the

371 pre-warmed culture medium for 3 times to release cells into mitosis and added with 1 ml of fresh
372 medium. Experiments were performed 40 minutes after the drug wash-off.

373 **Elastic polyacrylamide gel preparation**

374 The polyacrylamide gel used for cell compression was prepared as described in Matthews *et al*.
375 and Le Berre *et al*. with modifications (Le Berre et al., 2014; Matthews et al., 2020). Briefly, 18 mm
376 glass coverslips (Sangon, F518211) were treated with 10 μl Binding-silane (Sangon, C500226) for
377 10 minutes and then were rinsed with 100% ethanol and air-dried. To prepare soft elastic gels (2
378 kPa), 1 ml polyacrylamide gel solution was prepared by mixing 125 μl 40% w/v acrylamide
379 (Sangon), 35 μl 2% bis-arcylamide (Sangon), 10 μl APS (10% in water, Sangon), and 830 μl water.
380 After adding and mixing 1 μl TEMED (Sangon) into the gel solution, about 350 μl of the final gel
381 solution was immediately transferred onto a flat glass slide and covered by the coverslip pre-
382 treated with the Binding-silane. After polymerization for 20 minutes, the gel and the attached
383 coverslip were gently removed from the glass slide using a surgical blade and were soaked in PBS
384 for at least 2 hours and followed by incubation in cell culture media for overnight. In experiments
385 that involved drug treatment, the gels were incubated in media containing the drugs for overnight.

386 **Micropipette aspiration (MPA)**

387 The micropipette was prepared by first pulling a borosilicate glass capillary (Sutter Instrument,
388 B100-58-10) using the P-97 Micropipette puller (Sutter Instrument). Then, the thin end of a
389 borosilicate glass capillary was cut by a Microforge (Narishige) to a diameter of about 5.5 μm. The
390 micropipette was bent to a desired degree by heating it over an alcohol lamp and was filled with
391 phosphate-buffered saline (PBS) using the MicroFil (World Precision Instruments, MF34G-5). The
392 micropipette was installed to a micropipette holder, which was connected to a syringe pump
393 (Harvard apparatus) and a 25 ml serological plastic pipettes via a three-way valve. The
394 micropipette was positioned under an inverted microscope (Olympus, IX73) equipped with
395 Olympus 60x objective lens (N.A. 1.35, U Plan super apochromat), a micromanipulator system
396 (Eppendorf, TransferMan 4r), and a CMOS high speed camera (Vision Research, Phantom 410L,
397 333.33 nm / pixel).

398 To perform micropipette aspiration, cells were cultured on a one-well chambered coverglass
399 (Cellvis, C1-1.5H-N) for 24 hours and then were treated with 7.5 μM RO-3306 for 18 hours. Cells
400 were washed 3 times with fresh media and were added with fresh media containing 20 mM HEPES.
401 Cells were incubated for another 40 minutes to reach mitosis. When a mitotic cell was aspirated by
402 the micropipette, the microscopy image was captured and analyzed using Fiji to obtain the pipette
403 radius (R_p) and the cell radius (R_c). The cell length of about half a diameter of the pipette opening
404 was aspirated in. The water pressure changes (ΔP) as displayed on the 25 ml serological plastic
405 pipette was also recorded. Cell surface tension (T) was then calculated based on the Laplace
406 equation, $T = \Delta P / 2 (1/R_p - 1/R_c)$.

407 **Spinning-disk confocal microscopy for live-cell imaging**

408 Spinning-disk confocal microscopy was equipped with a Nikon Eclipse Ti2-E inverted microscope,
409 Nikon 60x oil-immersion objective lens (N.A. 1.40, Plan Apochromat Lambda), a spinning-disk
410 system (Yokogawa Electric Corporation, CSU-W1), a Photometrics Prime 95B sCMOS camera, a
411 Piezo Z stage (Physik Instrumente), and a live-cell stage top chamber with humidified CO_2
412 (Okolab). Images were acquired using the Metamorph with a z-step size of 0.5 μm and a x-y plane
413 resolution of 183.33 nm / pixel. The fluorophores were excited by laser lines at wavelengths of 488,
414 561, or 640 nm. For experiments involving cell compression, a z-stack of 30 μm was acquired
415 before cells were compressed and a stack of 22 μm was acquired after cells were compressed.
416 This ensured that the entire cell volume was covered during imaging.

417 **Mitotic cell compression and live-cell imaging**

418 To compress cells, 8 x 10^4 cells were first seeded on a 20 mm two-well chambered cover glass
419 (Cellvis, C2-1.5H-N). Forty-eight hours later, cells were treated with 7.5 μM RO-3306 to
420 synchronize cells at the G2/M boundary for 16 to 18 hours. Prior to live-cell imaging with
421 compression, synchronized cells were washed 3 times with the pre-warmed medium and added
422 with 1 ml of fresh medium and incubated in the stage-top chamber attached to the spinning-disk
423 microscopy for 40 minutes. When compressing the mitotic cells, the coverslip coated with the
424 elastic gel was put over the cell layer and followed by a 5 g weight. Elastic gels and weights were

425 pre-heated to 37 °C in the chamber. In experiments where cells were treated with DMSO, 20 μM
426 Y-27632 or 10 μM RO-3306, 1 ml medium containing 40 μM Y-27632 or 20 μM RO-3306 or
427 containing equivalent volume of DMSO was added to cells grown in 1 ml medium on the
428 chambered coverglass to achieve a final concentration of 20 μM Y-27632 or 10 μM RO-3306. The
429 elastic gel that was pre-incubated with 20 μM Y-27632 or 10 μM RO-3306 for overnight was then
430 put on top of the cell layer and followed by a 5 g weight. Cells at the same position were imaged
431 before and after compression. The cell compression efficiency was validated by their decrease of
432 cell heights. For microscopy imaging not involving cell compression, the μ-Slide 8-well chambered
433 coverglass (ibidi, 80826) was used for cell culture and imaging. Mitotic chromosomes were labeled
434 with 0.2 μM SiR-DNA in live cells during imaging (Cytoskeleton, CY-SC007).

435 **Image analysis and processing**

436 Microscopy images were analyzed using Fiji. To quantitate fluorescence intensity of mEmerald-
437 NMIIB, mRuby2-AHPH and dTomato-2xrGBD in mitotic cells (Figs. 1 C, 1 F, S1 E, S2 A) and in
438 mitotic cells for compression experiments (Figs. 2 E, 2 F, 3 B, 3 C, 3 D, 3 E, 4 E, 5 B, 5C, 5D, 6C),
439 image stacks containing 5 slices around the mid-plane were projected along the z-axis using the
440 sum-intensity projection (Fiji/image/stacks/Z project). Background subtraction (Fiji/process/subtract
441 background) was performed on projected images using the rolling ball radius of 20 pixels. Then, a
442 segmented line with a line width of 4 (for mitotic cells) or 5 (for mitotic cells in compression
443 experiments) was used to select the cortical fluorescent signals over the entire cell circumference.
444 The mean fluorescence intensity of the selected line region from the same cells before and after
445 treatment and/or compression was measured. The fold change was then calculated by dividing the
446 intensity after treatment and/or compression to the intensity before treatment and/or compression.
447 For time series in Fig. 1 B, the mean intensity of the cortical fluorescence was measured every 45
448 s. To quantitate the cell height in cell compression experiments, the number of slices from top to
449 bottom of a cell were multiplied by 0.5 μm.

450

451

452 **FRAP**

453 FRAP was performed using the above-mentioned spinning-disk confocal microscopy equipped with
454 Nikon 100x oil-immersion objective lens (N.A. 1.45, Plan Apochromat Lambda) and iLAS2 FRAP
455 system (Gataca). Images were acquired using the Metamorph software at 110 nm / pixel. The
456 mEmerald-NMIIB fluorescence signal was photobleached by using a short pulse of high power 488
457 nm laser lines and imaged by using a low power 488 nm laser lines. A small bleaching rectangular
458 region-of-interest (ROI) of about 2 x 10-μm was drawn on the cortical mEmerald-NMIIB in mitotic
459 cells. Three frames of pre-bleached images were acquired with 1 second interval before
460 photobleaching, followed by time-lapse imaging of the same cells with 2 seconds interval for 120
461 seconds. The bleaching ROIs were recorded to locate the regions of bleaching during analysis.

462 Fiji was used to quantitate the fluorescence intensity of FRAP images. Background subtraction
463 (Fiji/process/subtract background) was performed on the images with the rolling ball radius of 20
464 pixels. A segmented line ROI (line width 5) was used to select the FRAP regions for quantification.
465 The mean intensity of ROIs for pre-bleached images and after bleached images ($I_{bleached}$) was
466 calculated for each time point. A mean pre-bleached intensity ($I_{prebleach}$) was derived from the
467 average of three pre-bleached images. The ratio of $I_{bleached}$ / $I_{prebleach}$ at each time point was
468 calculated and was subsequently deducted by the ratio of the first image after photobleaching to
469 obtain $ratio_t$. The $ratio_t$ of each time point was plotted as the recovery curve and fitted using a non-
470 linear fitting function (one-phase association function constrained by Y0 = 0 and plateau < 1) in the
471 Prism 9 software (GraphPad). The recovery time was derived from the half-time parameter
472 calculated from the fitting. The mobile fraction was derived from the span parameter calculated
473 from the fitting. The immobile fraction was calculated as a difference between 1 and the mobile
474 fraction.

475 **Cytoskeletal fractionation**

476 Cells were washed once with ice-cold PBS. To a single well of a 6-well cell culture plate, 200 μl of
477 lysis buffer (50 mM PIPES, pH 6.8, 46 mM NaCl, 2.5 mM EGTA, 1 mM $MgCl_2$, 1mM ATP, 0.5%
478 Triton-X 100, protease inhibitor cocktail) was added. Lysates were harvested and centrifuged at

479 13000 *g* for 20 minutes at 4°C. The supernatant (soluble fraction) was separated from the pellet
480 (cytoskeletal fraction). The pellet was then resuspended in a same volume of lysis buffer as the
481 supernatant. Both fractions were added with 5 x Laemli sample buffer and boiled for 5 minutes.
482 The pellet suspension was sonicated in a water bath sonicator for 1 minute with 20% power to
483 improve solubility.

484 **Protein immunoblotting**

485 Protein samples were separated in a pre-cast SDS-PAGE gel (GenScript, M00657) and blotted to
486 a PVDF membrane (EMD Millipore, immobilon-P, IPVH00010). Blots were blocked with 5% skim
487 milk for 1 hour at room temperature and were incubated at 4°C overnight with the NMIIB antibody
488 (Proteintech, 19673-1-AP; used in Figs. 4 B and S3 A) or the β-actin antibody (HuaBio, ET1701-80;
489 used in Figs. 4 B and S1 C) or the GFP antibody (HuaBio, ET1604-26; used in Figs. 5 B C D and 6
490 A) or GAPDH antibody (Cell Signaling Technology, #5174; used in Fig. S3 A) or p-MLC2 antibody
491 (Cell Signaling Technology, #3675; used in Fig. S1 C). The secondary antibodies used were Alexa
492 Fluor Plus 800-conjugated goat anti-rabbit IgG secondary antibody (ThermoFisher, A32735) and
493 Alexa Fluor 680-conjugated goat anti-mouse IgG secondary antibody (ThermoFisher, A32729).
494 Blots were imaged using the LI-COR Odyssey CLx imaging system. The signal intensity of protein
495 bands was calculated using the LI-COR Image Studio software and Fiji. The cytoskeletal fraction
496 was calculated by dividing the cytoskeletal fraction intensity by the sum intensity of cytoskeletal
497 and soluble fractions. Protein band intensity measurements in Fig. 4 were obtained from four
498 proteins blots derived from four independent experiments. Protein band intensity measurements in
499 Fig. 5 and 6 were obtained from three proteins blots derived from three independent experiments.
500 The protein lysate in Fig. S1 A was prepared using Minute™ Total Protein Extraction Kit for Animal
501 Cultured Cells and Tissues (Invent Biotech, SD-001). Protein lysates used in protein blots in Figs.
502 4 and 5 and 6 and S3 were prepared using the cytoskeletal fractionation lysis buffer.

503 **Quantitative real-time PCR (qPCR) for checking endogenous NMIIB**

504 To validate the knockdown of endogenous NMIIB in cells used in Figs. 4 and 5 and 6, total RNAs
505 were prepared from cells using the FastPure Cell/Tissue Total RNA Isolation Kit (Vazyme, RC101-

506 01) and were reverse transcribed into cDNA using the HiScript II Q RT SuperMix for qPCR
507 (Vazyme, R223-01). The expression level of cDNAs was determined using the real-time PCR with
508 the ChamQ Universal SYBR qPCR Master Mix (Vazyme, Q711-02). The reaction mix was
509 assembled on the hard-shell PCR plate (Bio-Rad, HSP9655), sealed with the Microseal 'B' seal
510 (Bio-Rad, MSB1001), and was performed in the CFX96 Touch Real-Time PCR Detection System
511 (Bio-RAD, C1000). Primers used in the qPCR: GAPDH, 5' CAGGAGGCATTGCTGATGAT 3' and 5'
512 GAAGGCTGGGGCTCATTT 3'; NMIIB, 5' CCTCATGCTGACCTTGCAAA 3' and 5'
513 GGACACAAAACCAATATTCCCATT 3'. The primer pair for NMIIB targets the 3' UTR of NMIIB
514 gene, allowing checking of endogenous NMIIB expression. The C_T value for GAPDH was used for
515 normalization to obtain the relative expression level.

516 **Statistical analysis**

517 Statistical analysis was performed using Prism 9 (GraphPad). Datasets were analyzed by Student
518 t-test. If datasets were not normally distributed, they were analyzed using the Mann-Whitney test.
519 All graphs were plotted using Prism 9 (GraphPad).

520

521 **Author contributions**

522 C.W. and J.D. designed, performed experiments, and analyzed data. S.D. prepared elastic gels
523 used in the study. Q.W and X.G provided the devices and technical expertise for micropipette
524 aspiration. T.G.C conceived the study, designed experiments, supervised the study, and prepared
525 the manuscript with inputs from all authors.

526

527 **Acknowledgement**

528 This study was funded by Zhejiang University International Campus start-up grant (130000-
529 541902/016) and National Natural Science Foundation of China grant (32270770) given to T.G.C.
530 We thank Dr. Di Chen for sharing the CRISPRi vector with us. We thank Dr. Mikael Bjorklund for
531 sharing the 293Ta packaging cell line with us. We thank Dr. Wanzhong Ge and Dr. Junqi Huang

532 for their comments on the manuscript. Special thanks to Dr. Fang Kong from the Nanyang
533 Technological University, Singapore for designing the imaging chamber adaptor used in the
534 microscopy imaging for cell compression. Q.W and X.G would like to acknowledge the support
535 from the National Natural Science Foundation of China (12072198).

536

537 **Figure legends**

538 **Figure 1**. Establishment of a MCF10A cell line stably expressing mEmerald-NMIIB and mRuby2-
539 AHPH (active RhoA). (A) Micrographs of a representative cell showing mEmerald-NMIIB and
540 active RhoA localization during mitosis and cytokinesis. (B) Micrographs of the cortical mEmerald-
541 NMIIB in mitotic cells treated with different concentrations of p-nitroblebb. Cells before and 15
542 minutes after the treatments were shown. [Low] is 37 μM; [Medium] is 74 μM; [High] is 110 μM.
543 Insets show a zoom-in view of the punctate NMIIB. (C) Relative changes of cortical NMIIB intensity
544 as a function of time. The fluorescence intensity at each time point was normalized to that of in
545 cells before treatments. Dotted lines indicate standard deviation. DMSO, 12 cells; low, 9 cells;
546 medium, 9 cells; high, 10 cells. (D) Recovery curves of mEmerald-NMIIB fluorescence intensity
547 after photobleaching in cells treated with different concentrations of p-nitroblebb. DMSO, 36 cells;
548 low, 36 cells; medium, 30 cells; high, 28 cells. (E) Quantification of the recovery time and the
549 immobile fraction of mEmerald-NMIIB by FRAP. (F) Effect of C3 exoenzyme treatment on the
550 cortical NMIIB and active RhoA in a mitotic cell is shown. The changes of NMIIB and active RhoA
551 intensities at the mitotic cell cortex before and after 10 μg/ml C3 exoenyzme treatments were
552 quantified. The fold change is a ratio of the mean intensity after 10 μg/ml C3 exoenzyme treatment
553 to the mean intensity before treatment. The control group was added with media as C3 exoenzyme
554 was dissolved in water. NMIIB (control), 22 cells; NMIIB (C3 exoenzyme), 37 cells; active RhoA
555 (control), 35 cells; active RhoA (C3 exoenzyme), 36 cells.

556 Data represent means ± SD. Scale bar, 5 μm.

557

558 **Figure 2.** NMIIB and active RhoA show mechanoaccumulation at the cell cortex during mitosis. (A)
559 A schematic representation of the mitotic cell compression experiment. A soft elastic
560 polyacrylamide gel (2 kPa) was used in the study. (B) A representative cell before and after
561 compression is shown. XY, top view; XZ, side view. (C) Quantification of the cell height before and
562 after compression. 56 cells were counted for their cell height before and after compression. (D)
563 Two representative cells with increased accumulation of NMIIB at the cell cortex are shown. (E)
564 Intensity of the cortical NMIIB in mitotic cells before and after compression was quantitated. Black
565 dots indicate the intensity before compression and orange dots indicate the intensity after
566 compression of the same cells. 21 cells were counted. (F) Intensity of active RhoA in mitotic cells
567 before and after compression was quantitated. Black dots indicate the intensity before
568 compression and orange dots indicate the intensity after compression of the same cells. A
569 representative cell with increased cortical active RhoA after compression is shown. 26 cells were
570 counted. (G) Recovery curves of the cortical mEmerald-NMIIB intensity in uncompressed cells and
571 in compressed cells after photobleaching. Uncompressed, 55 cells; compressed, 48 cells. (H)
572 Quantification of the recovery time and the immobile fraction of mEmerald-NMIIB by FRAP.

573 Data represent means ± SD, except for (G) where data represent ± SEM. Scale bar, 5 μm.

574

575 **Figure 3**. Regulation of NMIIB mechanoresponse by ROCK and CDK1 signaling pathways. (A)
576 The cortical NMIIB and active RhoA at the cell cortex of mitotic cells before and after DMSO or 20
577 μM Y-27632 treatments or 10 μM RO-3306 are shown. (B) Quantification of the changes of NMIIB
578 and active RhoA intensities at the cell cortex before and after DMSO or 20 μM Y-27632 treatments.
579 (C) The fold change is a ratio of the mean intensity after treatments to the mean intensity before
580 treatment. A ratio higher than 1 means a positive mechanoresponse. NMIIB (DMSO), 26 cells;
581 NMIIB (Y-27632), 47 cells; active RhoA (DMSO), 30 cells; active RhoA (Y-27632), 55 cells. (D)
582 Quantification of the changes of NMIIB and active RhoA intensities at the cell cortex before and
583 after DMSO or 10 μM RO-3306 treatments. (E) The fold change is a ratio of the mean intensity
584 after treatments to the mean intensity before treatment. A ratio higher than 1 means a positive

585 mechanoresponse. NMIIB (DMSO), 27 cells; NMIIB (RO-3306), 27 cells; active RhoA (DMSO), 24
586 cells; active RhoA (RO-3306), 25 cells.

587 Data represent means ± SD. Scale bar, 5 μm.

588

589 **Figure 4.** Perturbation of the NMIIB tail domain regulation affects maintenance of the mitotic cell
590 surface tension but less on the NMIIB mechanoresponse. (A) A schematic representation of the
591 phosphoregulation of the NMIIB tail regrion in controlling the myosin II filament assembly. (B) A
592 protein blot shows the cytoskeletal fractions and soluble fractions of NMIIB and actin in MCF10A
593 cells expressing different phosphomutants in the absence of endogenous NMIIB. KD, knockdown.
594 (C) Quantification of the cytoskeletal fractions of NMIIB wild type or phosphomutants from the
595 protein blot. (D) Measurement of the mitotic cell surface tension by MPA in cells expressing NMIIB
596 (WT), NMIIB (S1935A), or NMIIB (S1935D). NMIIB (WT), 59 cells; NMIIB (S1935A), 40 cells;
597 NMIIB(S1935D), 40 cells. (E) Quantification of the changes of NMIIB (WT), NMIIB (S1935A), and
598 NMIIB (S1935D) at the cell cortex before and after compression. The fold change is a ratio of the
599 mean intensity after compression to the mean intensity before compression. The dotted indicates
600 ratio of 1 in which a ratio higher than 1 means a positive mechanoresponse. NMIIB (WT), 30 cells;
601 NMIIB (S1935A), 28 cells; NMIIB (S1935D), 28 cells.

602 Data represent means ± SD. Scale bar, 5 μm.

603

604 **Figure 5**. NMIIB that is motor-dead but retaining actin-binding function is defective in
605 mechanoaccumulation. (A) A diagram showing the motor activity mutations and actin-binding
606 mutations of NMIIB used in the study. (B) Left panel, micrographs of a cell expressing wild type
607 NMIIB (NMIIB-WT) and a cell expressing NMIIB-R709C before and after compression; middle
608 panel, the fold change is a ratio of the mean intensity after compression to the mean intensity
609 before compression. A ratio higher than 1 means a positive mechanoresponse.NMIIB WT, 53 cells;
610 NMIIB (R709C), 60 cells; right panel, a protein blot and quantification of the cytoskeletal fractions
611 and soluble fractions of NMIIB wild type and NMIIB (R709C) mutant proteins. (C) Left panel,

612 micrographs of a cell expressing wild type NMIIB (NMIIB-WT) and a cell expressing NMIIB-R241A
613 before and after compression; middle panel, the fold change is a ratio of the mean intensity after
614 compression to the mean intensity before compression. A ratio higher than 1 means a positive
615 mechanoresponse. NMIIB WT, 51 cells; NMIIB (R241A), 46 cells; right panel, a protein blot and
616 quantification of the cytoskeletal fractions and soluble fractions of NMIIB wild type and NMIIB
617 (R241A) mutant proteins. (D) Left panel, micrographs of a cell expressing wild type NMIIB (NMIIB-
618 WT) and a cell expressing NMIIB-K647A before and after compression; middle panel, the fold
619 change is a ratio of the mean intensity after compression to the mean intensity before compression.
620 A ratio higher than 1 means a positive mechanoresponse. NMIIB WT, 50 cells; NMIIB (K647A), 54
621 cells; right panel, a protein blot and quantification of the cytoskeletal fractions and soluble fractions
622 of NMIIB wild type and NMIIB (K647A) mutant proteins.

623 Data represent means ± SD. Scale bar, 5 μm.

624

625 **Figure 6**. The translocation activity plays a dominant role in regulating NMIIB
626 mechanoaccumulation. (A) Protein blots and quantification of the cytoskeletal fractions and soluble
627 fractions of NMIIB wild type and NMIIB double mutant proteins. (B) Micrographs of cells expressing
628 wild type NMIIB or NMIIB double mutants before and after compression. (C) The fold change is a
629 ratio of the mean intensity after compression to the mean intensity before compression. A ratio
630 higher than 1 means a positive mechanoresponse. NMIIB WT, 43 cells; NMIIB (S1935D), 48 cells;
631 NMIIB (R709C S1935D), 43 cells; NMIIB (R241A S1935D), 32 cells; NMIIB (K647A S1935D), 40
632 cells.

633 Data represent means ± SD. Scale bar, 5 μm.

634

635 **Figure S1**. (A) Increased accumulation of NMIIB and active RhoA at the mitotic cell cortex in the
636 same individual cells. Fold changes of NMIIB and active RhoA at the mitotic cell cortex after
637 compression in individual cells were plotted. (B) Intensity of active RhoA in mitotic cells expressing
638 dTomato-2xrGBD (Rhotekin GBD) before and after compression was quantitated. Black dots

639 indicate the intensity before compression and orange dots indicate the intensity after compression
640 of the same cells. A representative cell with increased cortical active RhoA after compression is
641 shown. 29 cells were counted. (C) Protein blots showing levels of phosphorylated myosin light
642 chain and actin in uncompressed and compressed cells. (D) Measurement of the mitotic cell
643 surface tension by MPA in the presence of different concentrations of p-nitroblebb. The inset
644 shows an example of an aspirated cell. DMSO, 33 cells; low, 40 cells; medium, 39 cells; high, 43
645 cells. (E) Relative changes of active RhoA intensity at the cell cortex after DMSO or 110 μM p-
646 nitroblebb treatments as a function of time. The fluorescence intensity at each time point was
647 normalized to that of in cells before treatments. DMSO, 11 cells; p-nitroblebb, 17 cells.
648 Representative cells showing the decrease of active RhoA at the mitotic cell cortex before and
649 after p-nitroblebb treatment are shown.

650 Data represent means ± SD. Scale bar, 5 μm.

651

652 **Figure S2**. (A) The cortical NMIIB and active RhoA at the cell cortex of mitotic cells before and
653 after DMSO, 20 μM Y-27632 or 10 μM RO-3306 treatments are shown. (B) Quantification of the
654 changes of NMIIB and active RhoA intensities at the cell cortex before and after DMSO or 20 μM
655 Y-27632 treatments. The fold change is a ratio of the mean intensity after treatments to the mean
656 intensity before treatment. NMIIB (DMSO), 26 cells; NMIIB (Y-27632), 47 cells; NMIIB (RO-3306),
657 24 cells; active RhoA (DMSO), 30 cells; active RhoA (Y-27632), 55 cells; active RhoA (RO-3306),
658 35 cells. A ratio higher than 1 means increased intensity after treatments. (C) Measurement of the
659 mitotic cell surface tension by MPA in cells treated with DMSO, 20 μM Y-27632, or 10 μM RO-
660 3306. DMSO, 59 cells; Y-27632, 59 cells; RO-3306, 60 cells. (D) Quantification of the cell height
661 before and after treatment of DMSO, 20 μM Y-27632, or 10 μM RO-3306 with compression. 25
662 cells in each DMSO or Y-27632 treatment and compression were counted for their cell heights. 27
663 cells in each DMSO or RO-3306 treatment and compression were counted for their cell heights.

664 Data represent means ± SD. Scale bar, 5 μm.

665 **Figure S3.** Identification of gRNA sequences that could knockdown NMIIB expression by CRISPRi.
666 (A) Western blotting shows the knockdown efficiency of endogenous NMIIB by CRISPRi using 3
667 different guiding RNAs (gRNAs). Highlighted gRNA 3 was used in the study to knock down NMIIB.
668 (B) Relative expression of endogenous NMIIB in MCF10A cells, MCF10A cells expressing wild
669 type NMIIB or phosphomutants as determined by qPCR. (C) Quantification of the cell height in
670 cells expressing NMIIB (WT), NMIIB (S1935A), or NMIIB (S1935D) before and after compression.
671 NMIIB (WT), 30 cells; NMIIB (S1935A), 21 cells, NMIIB (S1935D), 26 cells.

672 Data represent means ± SD.

673

674 **References**

675 Acharya, B.R., A. Nestor-Bergmann, X. Liang, S. Gupta, K. Duszyc, E. Gauquelin, G.A. Gomez, S. Budnar, P.
676 Marcq, O.E. Jensen, Z. Bryant, and A.S. Yap. 2018. A Mechanosensitive RhoA Pathway that Protects
677 Epithelia against Acute Tensile Stress. *Dev Cell*. 47:439-452 e436.
678 Amano, M., M. Ito, K. Kimura, Y. Fukata, K. Chihara, T. Nakano, Y. Matsuura, and K. Kaibuchi. 1996.
679 Phosphorylation and activation of myosin by Rho-associated kinase (Rho-kinase). *J Biol Chem*.
680 271:20246-20249.
681 Beaudet, D., N. Pham, N. Skaik, and A. Piekny. 2020. Importin binding mediates the intramolecular
682 regulation of anillin during cytokinesis. *Mol Biol Cell*. 31:1124-1139.
683 Bischof, J., C.A. Brand, K. Somogyi, I. Majer, S. Thome, M. Mori, U.S. Schwarz, and P. Lenart. 2017. A cdk1
684 gradient guides surface contraction waves in oocytes. *Nat Commun*. 8:849.
685 Cadart, C., E. Zlotek-Zlotkiewicz, M. Le Berre, M. Piel, and H.K. Matthews. 2014. Exploring the function of
686 cell shape and size during mitosis. *Dev Cell*. 29:159-169.
687 Cattin, C.J., M. Duggelin, D. Martinez-Martin, C. Gerber, D.J. Muller, and M.P. Stewart. 2015. Mechanical
688 control of mitotic progression in single animal cells. *Proc Natl Acad Sci U S A*. 112:11258-11263.
689 Cavanaugh, K.E., M.F. Staddon, T.A. Chmiel, R. Harmon, S. Budnar, A.S. Yap, S. Banerjee, and M.L. Gardel.
690 2022. Force-dependent intercellular adhesion strengthening underlies asymmetric adherens
691 junction contraction. *Curr Biol*. 32:1986-2000 e1985.
692 Chew, T.G., J. Huang, S. Palani, R. Sommese, A. Kamnev, T. Hatano, Y. Gu, S. Oliferenko, S. Sivaramakrishnan,
693 and M.K. Balasubramanian. 2017. Actin turnover maintains actin filament homeostasis during
694 cytokinetic ring contraction. *J Cell Biol*. 216:2657-2667.
695 Choi, C.K., M. Vicente-Manzanares, J. Zareno, L.A. Whitmore, A. Mogilner, and A.R. Horwitz. 2008. Actin and
696 alpha-actinin orchestrate the assembly and maturation of nascent adhesions in a myosin II motor-
697 independent manner. *Nat Cell Biol*. 10:1039-1050.
698 Debold, E.P. 2021. Recent insights into the relative timing of myosin's powerstroke and release of
699 phosphate. *Cytoskeleton (Hoboken)*. 78:448-458.
700 Garrido-Casado, M., G. Asensio-Juarez, and M. Vicente-Manzanares. 2021. Nonmuscle Myosin II Regulation
701 Directs Its Multiple Roles in Cell Migration and Division. *Annu Rev Cell Dev Biol*. 37:285-310.
702 Guilluy, C., V. Swaminathan, R. Garcia-Mata, E.T. O'Brien, R. Superfine, and K. Burridge. 2011. The Rho GEFs
703 LARG and GEF-H1 regulate the mechanical response to force on integrins. *Nat Cell Biol*. 13:722-727.
704 Heissler, S.M., and J.R. Sellers. 2016. Various Themes of Myosin Regulation. *J Mol Biol*. 428:1927-1946.

705 Juanes-Garcia, A., J.R. Chapman, R. Aguilar-Cuenca, C. Delgado-Arevalo, J. Hodges, L.A. Whitmore, J.
706 Shabanowitz, D.F. Hunt, A.R. Horwitz, and M. Vicente-Manzanares. 2015. A regulatory motif in
707 nonmuscle myosin II-B regulates its role in migratory front-back polarity. *J Cell Biol*. 209:23-32.
708 Kasza, K.E., S. Supriyatno, and J.A. Zallen. 2019. Cellular defects resulting from disease-related myosin II
709 mutations in Drosophila. *Proc Natl Acad Sci U S A*. 116:22205-22211.
710 Kelkar, M., P. Bohec, and G. Charras. 2020. Mechanics of the cellular actin cortex: From signalling to shape
711 change. *Curr Opin Cell Biol*. 66:69-78.
712 Kepiro, M., B.H. Varkuti, L. Vegner, G. Voros, G. Hegyi, M. Varga, and A. Malnasi-Csizmadia. 2014. para-
713 Nitroblebbistatin, the non-cytotoxic and photostable myosin II inhibitor. *Angew Chem Int Ed Engl*.
714 53:8211-8215.
715 Kim, K.Y., M. Kovacs, S. Kawamoto, J.R. Sellers, and R.S. Adelstein. 2005. Disease-associated mutations and
716 alternative splicing alter the enzymatic and motile activity of nonmuscle myosins II-B and II-C. *J Biol*
717 *Chem*. 280:22769-22775.
718 Koh, S.P., N.P. Pham, and A. Piekny. 2021. Seeing is believing: tools to study the role of Rho GTPases during
719 cytokinesis. *Small GTPases*:1-14.
720 Lancaster, O.M., M. Le Berre, A. Dimitracopoulos, D. Bonazzi, E. Zlotek-Zlotkiewicz, R. Picone, T. Duke, M.
721 Piel, and B. Baum. 2013. Mitotic rounding alters cell geometry to ensure efficient bipolar spindle
722 formation. *Dev Cell*. 25:270-283.
723 Le Berre, M., E. Zlotek-Zlotkiewicz, D. Bonazzi, F. Lautenschlaeger, and M. Piel. 2014. Methods for two-
724 dimensional cell confinement. *Methods Cell Biol*. 121:213-229.
725 Luo, T., K. Mohan, P.A. Iglesias, and D.N. Robinson. 2013. Molecular mechanisms of cellular
726 mechanosensing. *Nat Mater*. 12:1064-1071.
727 Ma, X., M. Kovacs, M.A. Conti, A. Wang, Y. Zhang, J.R. Sellers, and R.S. Adelstein. 2012. Nonmuscle myosin II
728 exerts tension but does not translocate actin in vertebrate cytokinesis. *Proc Natl Acad Sci U S A*.
729 109:4509-4514.
730 Maddox, A.S., and K. Burridge. 2003. RhoA is required for cortical retraction and rigidity during mitotic cell
731 rounding. *J Cell Biol*. 160:255-265.
732 Mahlandt, E.K., J.J.G. Arts, W.J. van der Meer, F.H. van der Linden, S. Tol, J.D. van Buul, T.W.J. Gadella, and J.
733 Goedhart. 2021. Visualizing endogenous Rho activity with an improved localization-based,
734 genetically encoded biosensor. *J Cell Sci*. 134.
735 Matthews, H.K., U. Delabre, J.L. Rohn, J. Guck, P. Kunda, and B. Baum. 2012. Changes in Ect2 localization
736 couple actomyosin-dependent cell shape changes to mitotic progression. *Dev Cell*. 23:371-383.
737 Matthews, H.K., S. Ganguli, K. Plak, A.V. Taubenberger, Z. Win, M. Williamson, M. Piel, J. Guck, and B. Baum.
738 2020. Oncogenic Signaling Alters Cell Shape and Mechanics to Facilitate Cell Division under
739 Confinement. *Dev Cell*. 52:563-573 e563.
740 Murrell, M., P.W. Oakes, M. Lenz, and M.L. Gardel. 2015. Forcing cells into shape: the mechanics of
741 actomyosin contractility. *Nat Rev Mol Cell Biol*. 16:486-498.
742 Nayak, A., T. Wang, P. Franz, W. Steffen, I. Chizhov, G. Tsiavaliaris, and M. Amrute-Nayak. 2020. Single-
743 molecule analysis reveals that regulatory light chains fine-tune skeletal myosin II function. *J Biol*
744 *Chem*. 295:7046-7059.
745 Nguyen, L.T.S., M.A.C. Jacob, E. Parajon, and D.N. Robinson. 2022. Cancer as a biophysical disease:
746 Targeting the mechanical-adaptability program. *Biophys J*. 121:3573-3585.
747 Nia, H.T., L.L. Munn, and R.K. Jain. 2020. Physical traits of cancer. *Science*. 370.
748 Nishimura, K., Y. Johmura, K. Deguchi, Z. Jiang, K.S.K. Uchida, N. Suzuki, M. Shimada, Y. Chiba, T. Hirota, S.H.
749 Yoshimura, K. Kono, and M. Nakanishi. 2019. Cdk1-mediated DIAPH1 phosphorylation maintains
750 metaphase cortical tension and inactivates the spindle assembly checkpoint at anaphase. *Nat*
751 *Commun*. 10:981.
752 Onishi, H., S.V. Mikhailenko, and M.F. Morales. 2006. Toward understanding actin activation of myosin
753 ATPase: the role of myosin surface loops. *Proc Natl Acad Sci U S A*. 103:6136-6141.
754 Osorio, D.S., F.Y. Chan, J. Saramago, J. Leite, A.M. Silva, A.F. Sobral, R. Gassmann, and A.X. Carvalho. 2019.
755 Crosslinking activity of non-muscle myosin II is not sufficient for embryonic cytokinesis in C. elegans.
756 *Development*. 146.
757 Piekny, A.J., and M. Glotzer. 2008. Anillin is a scaffold protein that links RhoA, actin, and myosin during
758 cytokinesis. *Curr Biol*. 18:30-36.

759 Priya, R., G.A. Gomez, S. Budnar, S. Verma, H.L. Cox, N.A. Hamilton, and A.S. Yap. 2015. Feedback regulation
760 through myosin II confers robustness on RhoA signalling at E-cadherin junctions. *Nat Cell Biol*.
761 17:1282-1293.
762 Ramanathan, S.P., J. Helenius, M.P. Stewart, C.J. Cattin, A.A. Hyman, and D.J. Muller. 2015. Cdk1-dependent
763 mitotic enrichment of cortical myosin II promotes cell rounding against confinement. *Nat Cell Biol*.
764 17:148-159.
765 Ramkumar, N., and B. Baum. 2016. Coupling changes in cell shape to chromosome segregation. *Nat Rev*
766 *Mol Cell Biol*. 17:511-521.
767 Rauscher, A.A., M. Gyimesi, M. Kovacs, and A. Malnasi-Csizmadia. 2018. Targeting Myosin by Blebbistatin
768 Derivatives: Optimization and Pharmacological Potential. *Trends Biochem Sci*. 43:700-713.
769 Rosa, A., E. Vlassaks, F. Pichaud, and B. Baum. 2015. Ect2/Pbl acts via Rho and polarity proteins to direct the
770 assembly of an isotropic actomyosin cortex upon mitotic entry. *Dev Cell*. 32:604-616.
771 Schiffhauer, E.S., T. Luo, K. Mohan, V. Srivastava, X. Qian, E.R. Griffis, P.A. Iglesias, and D.N. Robinson. 2016.
772 Mechanoaccumulative Elements of the Mammalian Actin Cytoskeleton. *Curr Biol*. 26:1473-1479.
773 Schiffhauer, E.S., Y. Ren, V.A. Iglesias, P. Kothari, P.A. Iglesias, and D.N. Robinson. 2019. Myosin IIB assembly
774 state determines its mechanosensitive dynamics. *J Cell Biol*. 218:895-908.
775 Smutny, M., H.L. Cox, J.M. Leerberg, E.M. Kovacs, M.A. Conti, C. Ferguson, N.A. Hamilton, R.G. Parton, R.S.
776 Adelstein, and A.S. Yap. 2010. Myosin II isoforms identify distinct functional modules that support
777 integrity of the epithelial zonula adherens. *Nat Cell Biol*. 12:696-702.
778 Stewart, M.P., J. Helenius, Y. Toyoda, S.P. Ramanathan, D.J. Muller, and A.A. Hyman. 2011. Hydrostatic
779 pressure and the actomyosin cortex drive mitotic cell rounding. *Nature*. 469:226-230.
780 Sweeney, H.L., and A. Houdusse. 2010. Structural and functional insights into the Myosin motor mechanism.
781 *Annu Rev Biophys*. 39:539-557.
782 Taneja, N., M.R. Bersi, S.M. Baillargeon, A.M. Fenix, J.A. Cooper, R. Ohi, V. Gama, W.D. Merryman, and D.T.
783 Burnette. 2020. Precise Tuning of Cortical Contractility Regulates Cell Shape during Cytokinesis. *Cell*
784 *Rep*. 31:107477.
785 Trivedi, D.V., J.M. Muretta, A.M. Swenson, J.P. Davis, D.D. Thomas, and C.M. Yengo. 2015. Direct
786 measurements of the coordination of lever arm swing and the catalytic cycle in myosin V. *Proc Natl*
787 *Acad Sci U S A*. 112:14593-14598.
788 Vicente-Manzanares, M., X. Ma, R.S. Adelstein, and A.R. Horwitz. 2009. Non-muscle myosin II takes centre
789 stage in cell adhesion and migration. *Nat Rev Mol Cell Biol*. 10:778-790.
790 von der Ecken, J., S.M. Heissler, S. Pathan-Chhatbar, D.J. Manstein, and S. Raunser. 2016. Cryo-EM structure
791 of a human cytoplasmic actomyosin complex at near-atomic resolution. *Nature*. 534:724-728.
792 Wulf, S.F., V. Ropars, S. Fujita-Becker, M. Oster, G. Hofhaus, L.G. Trabuco, O. Pylypenko, H.L. Sweeney, A.M.
793 Houdusse, and R.R. Schroder. 2016. Force-producing ADP state of myosin bound to actin. *Proc Natl*
794 *Acad Sci U S A*. 113:E1844-1852.

795

Figure 1

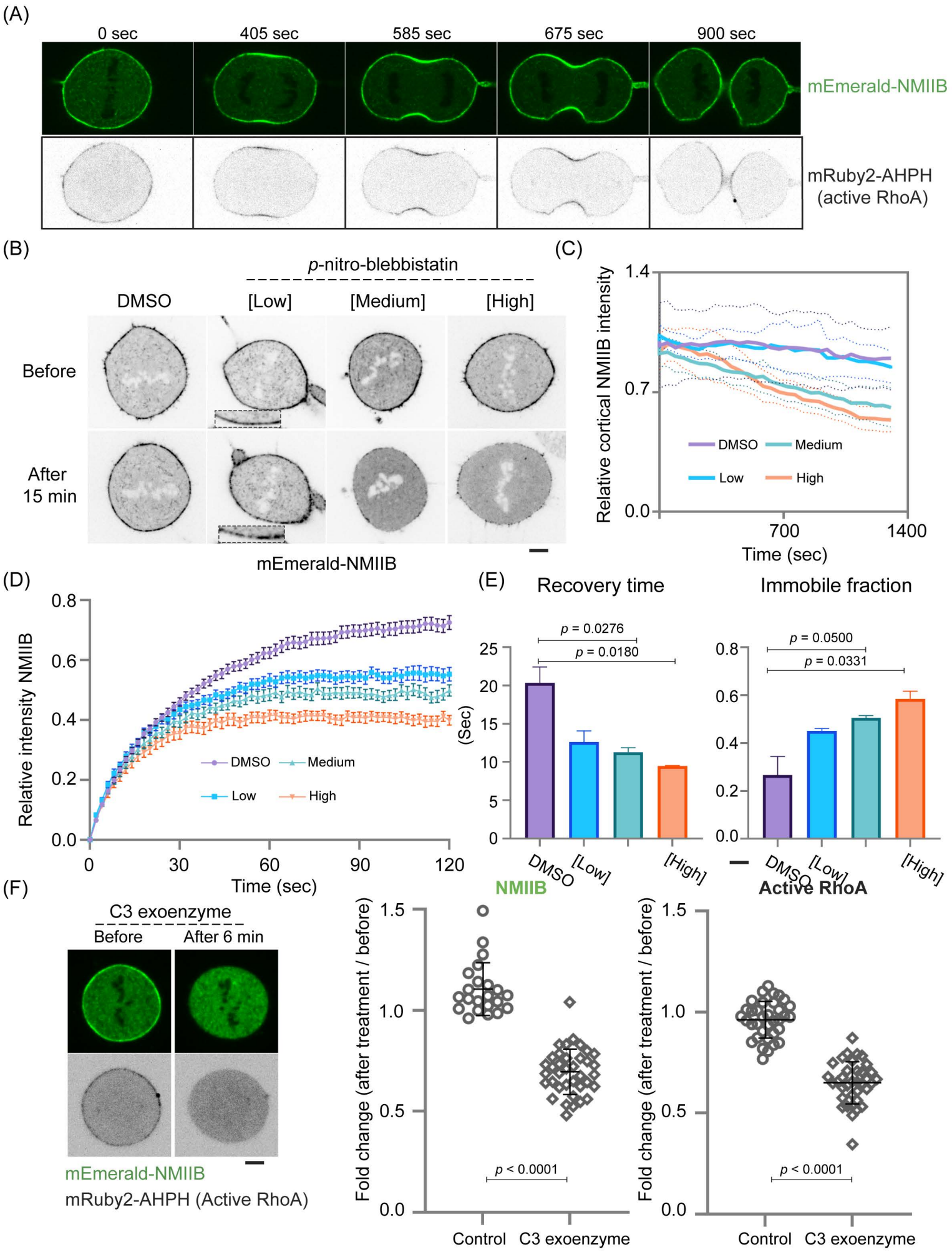
(A)
0 sec
405 sec
585 sec
675 sec
900 sec
mEmerald-NMIIB
mRuby2-AHPH
(active RhoA)
(B)
p-nitro-blebbistatin
DMSO
[Low]
[Medium]
[High]
Before
After
15 min
mEmerald-NMIIB
(C)
Relative cortical NMIIB intensity
1.4
0.7
0.0
700
1400
Time (sec)
DMSO
Medium
Low
High
(D)
Relative intensity NMIIB
0.8
0.6
0.4
0.2
0.0
0
30
60
90
120
Time (sec)
DMSO
Medium
Low
High
(E)
Recovery time
Immobile fraction
p = 0.0276
p = 0.0180
(Sec)
25
20
15
10
5
0
DMSO
[Low]
[High]
NMIIB
p = 0.0500
p = 0.0331
0.8
0.6
0.4
0.2
0.0
DMSO
[Low]
[High]
Active RhoA
(F)
C3 exoenzyme
Before
After 6 min
mEmerald-NMIIB
mRuby2-AHPH (Active RhoA)
Fold change (after treatment / before)
1.5
1.0
0.5
0.0
p < 0.0001
Control
C3 exoenzyme
Fold change (after treatment / before)
1.5
1.0
0.5
0.0
p < 0.0001
Control
C3 exoenzyme

Figure 2

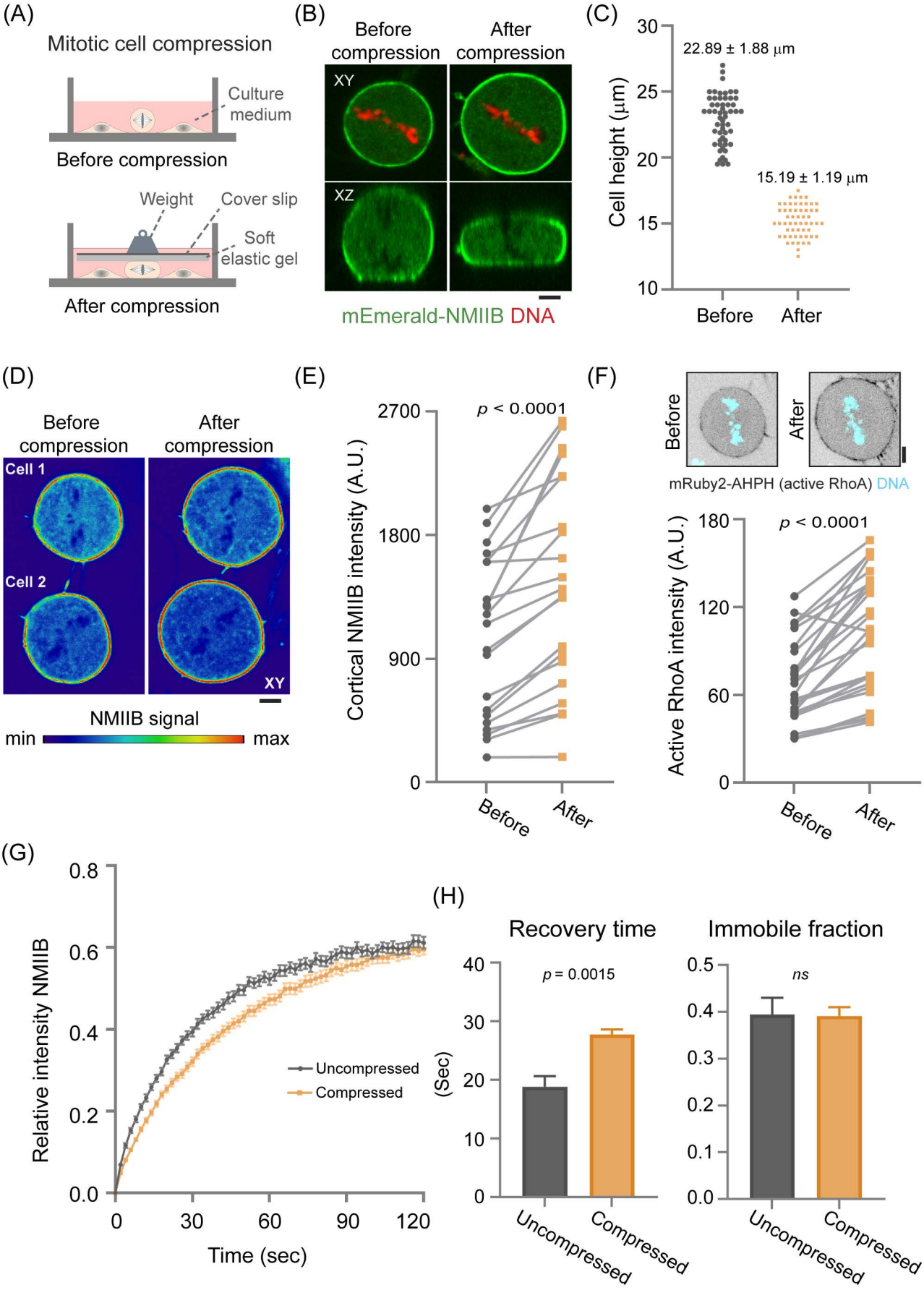
(A)
Mitotic cell compression
Culture medium
Before compression
Weight
Cover slip
Soft elastic gel
After compression
(B)
Before compression
After compression
XY
XZ
mEmerald-NMIIB DNA
(C)
22.89 ± 1.88 μm
15.19 ± 1.19 μm
Cell height (μm)
30
25
20
15
10
Before
After
(D)
Before compression
After compression
Cell 1
Cell 2
XY
NMIIB signal
min
max
(E)
p < 0.0001
Cortical NMIIB intensity (A.U.)
2700
1800
900
0
Before
After
(F)
Before
After
mRuby2-AHPH (active RhoA) DNA
p < 0.0001
Active RhoA intensity (A.U.)
180
120
60
0
Before
After
(G)
Relative intensity NMIIB
0.8
0.6
0.4
0.2
0.0
Uncompressed
Compressed
0
30
60
90
120
Time (sec)
(H)
Recovery time
p = 0.0015
(Sec)
40
30
20
10
0
Uncompressed
Compressed
Immobile fraction
ns
0.5
0.4
0.3
0.2
0.1
0.0
Uncompressed
Compressed

Figure 3

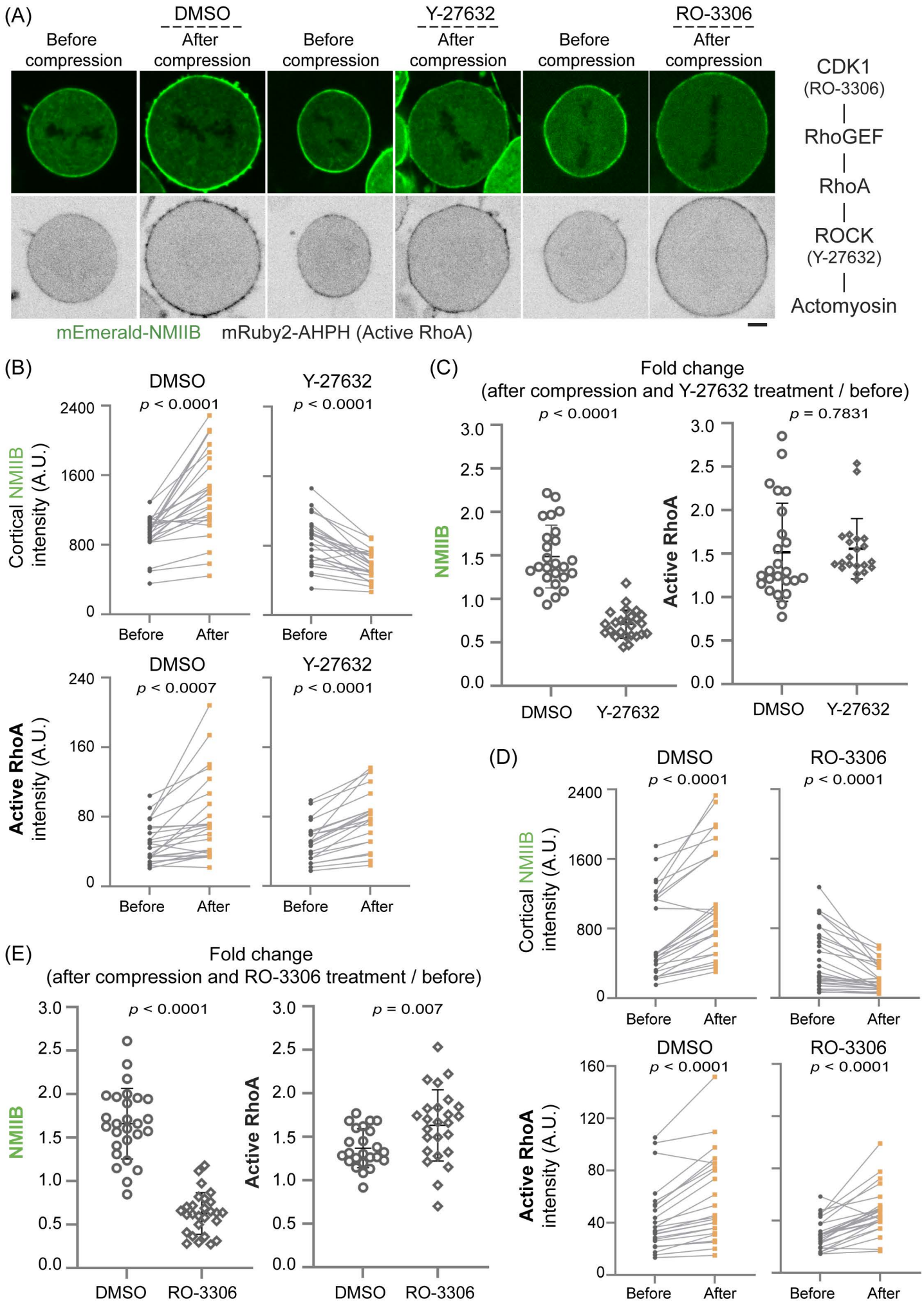
(A)
DMSO
Y-27632
RO-3306
Before compression
After compression
Before compression
After compression
Before compression
After compression
CDK1
(RO-3306)
RhoGEF
RhoA
ROCK
(Y-27632)
Actomyosin
mEmerald-NMIIB
mRuby2-AHPH (Active RhoA)
(B)
DMSO
Y-27632
p < 0.0001
p < 0.0001
Cortical NMIIB intensity (A.U.)
2400
1600
800
0
Before
After
DMSO
Y-27632
p < 0.0007
p < 0.0001
Active RhoA intensity (A.U.)
240
160
80
0
Before
After
(C)
Fold change
(after compression and Y-27632 treatment / before)
p < 0.0001
p = 0.7831
NMIIB
Active RhoA
3.0
2.5
2.0
1.5
1.0
0.5
0.0
DMSO
Y-27632
(D)
DMSO
RO-3306
p < 0.0001
p < 0.0001
Cortical NMIIB intensity (A.U.)
2400
1600
800
0
Before
After
DMSO
RO-3306
p < 0.0001
p < 0.0001
Active RhoA intensity (A.U.)
160
120
80
40
0
Before
After
(E)
Fold change
(after compression and RO-3306 treatment / before)
p < 0.0001
p = 0.007
NMIIB
Active RhoA
3.0
2.5
2.0
1.5
1.0
0.5
0.0
DMSO
RO-3306

Figure 4

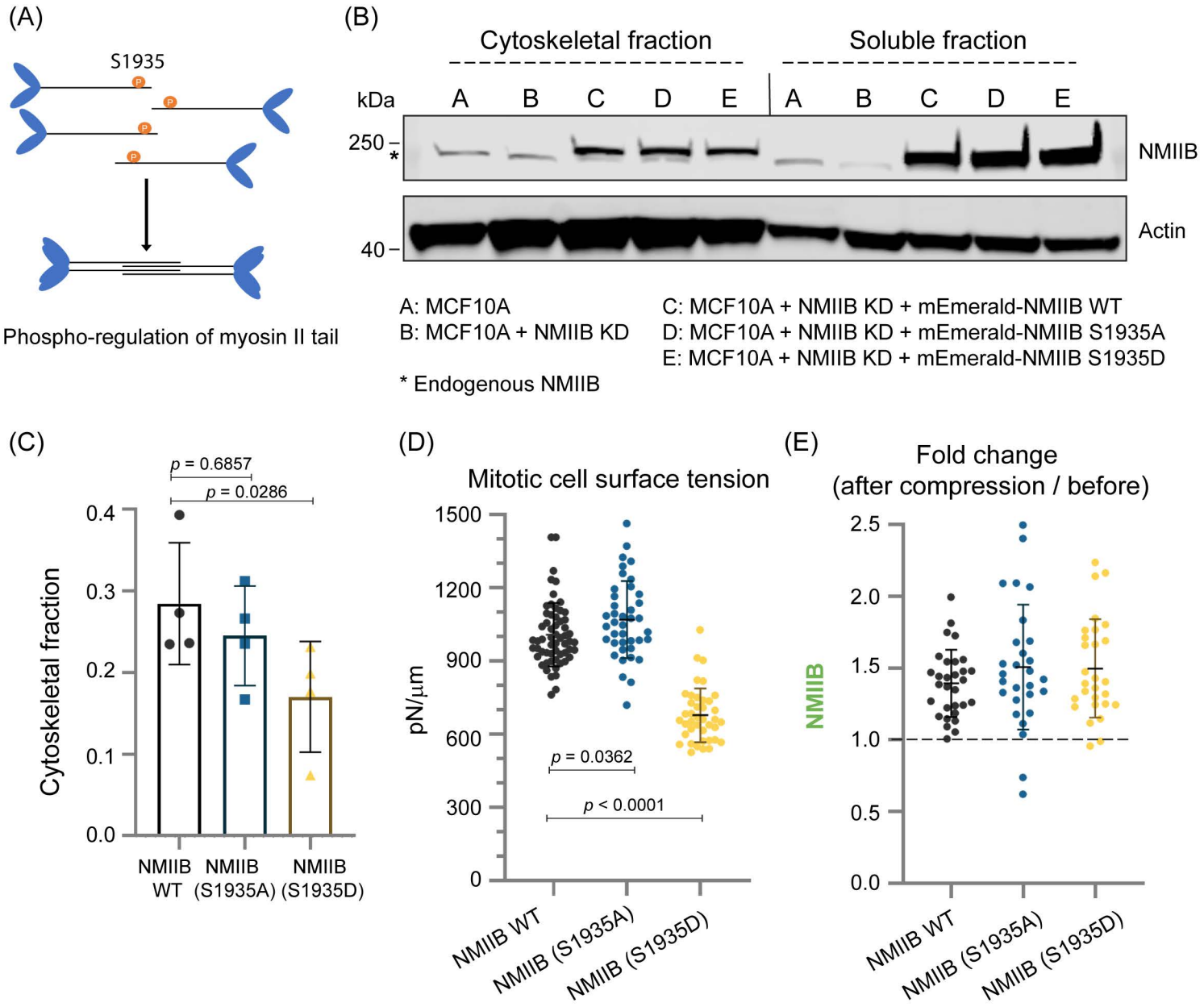
(A)
S1935
Phospho-regulation of myosin II tail
(B)
Cytoskeletal fraction
Soluble fraction
kDa
A B C D E A B C D E
250
*
40
NMIIB
Actin
A: MCF10A
B: MCF10A + NMIIB KD
C: MCF10A + NMIIB KD + mEmerald-NMIIB WT
D: MCF10A + NMIIB KD + mEmerald-NMIIB S1935A
E: MCF10A + NMIIB KD + mEmerald-NMIIB S1935D
* Endogenous NMIIB
(C)
p = 0.6857
p = 0.0286
Cytoskeletal fraction
0.0
0.1
0.2
0.3
0.4
NMIIB WT
NMIIB (S1935A)
NMIIB (S1935D)
(D)
Mitotic cell surface tension
pN/µm
0
300
600
900
1200
1500
p = 0.0362
p < 0.0001
NMIIB WT
NMIIB (S1935A)
NMIIB (S1935D)
(E)
Fold change
(after compression / before)
NMIIB
0.0
0.5
1.0
1.5
2.0
2.5
NMIIB WT
NMIIB (S1935A)
NMIIB (S1935D)

Figure 5

(A)

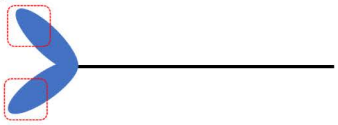

Motor activity mutation: S241A, R709C
Actin binding mutation: K647A

(B)

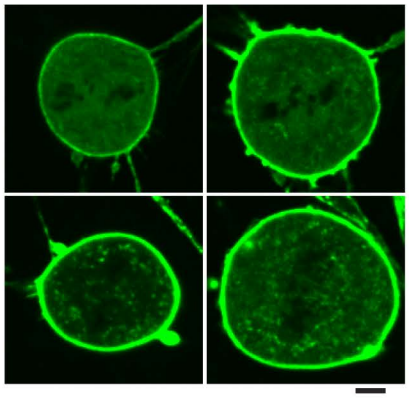

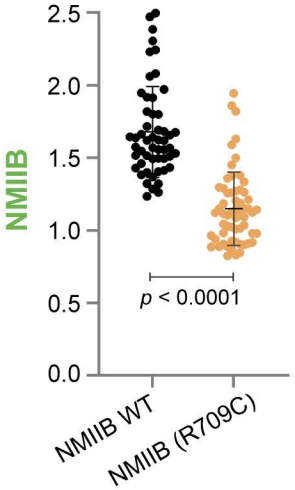

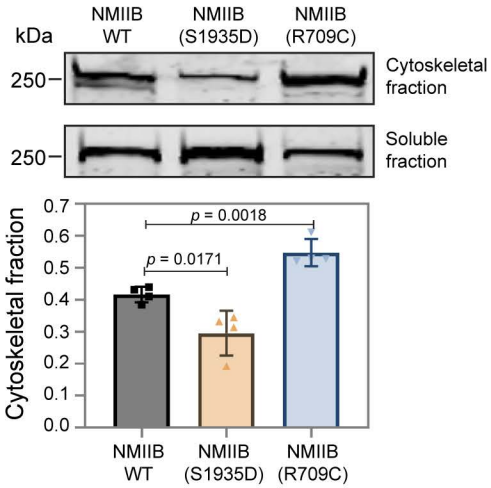

(C)

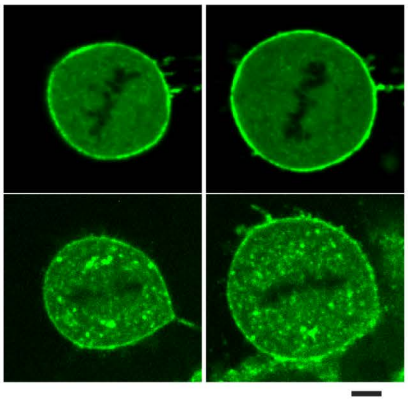

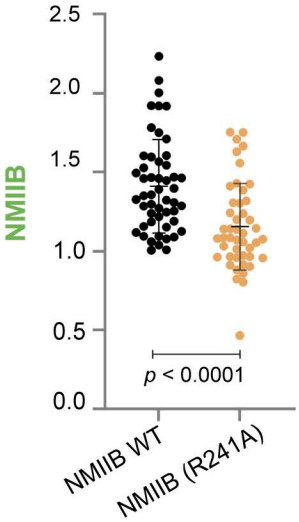

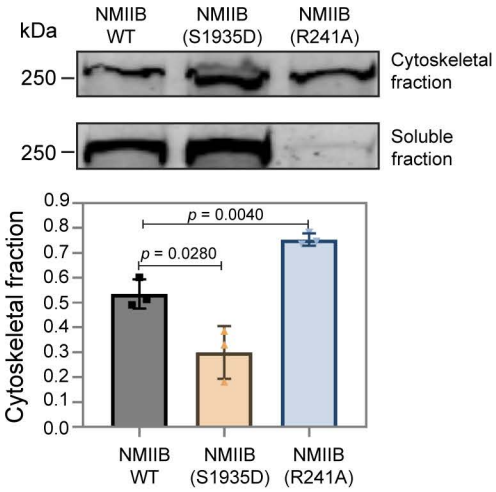

(D)

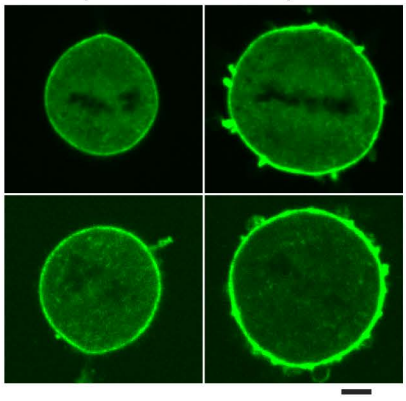

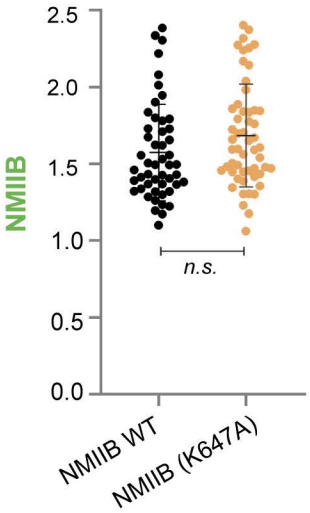

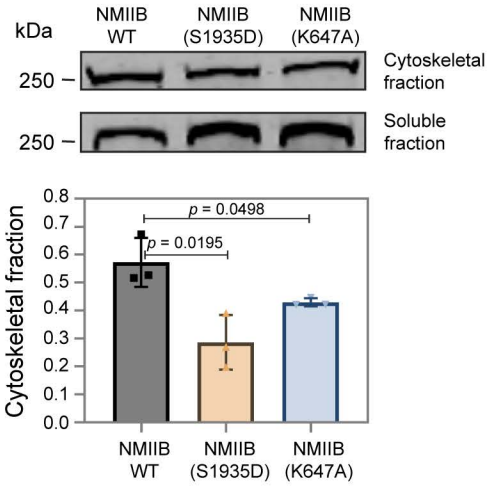

Figure 6

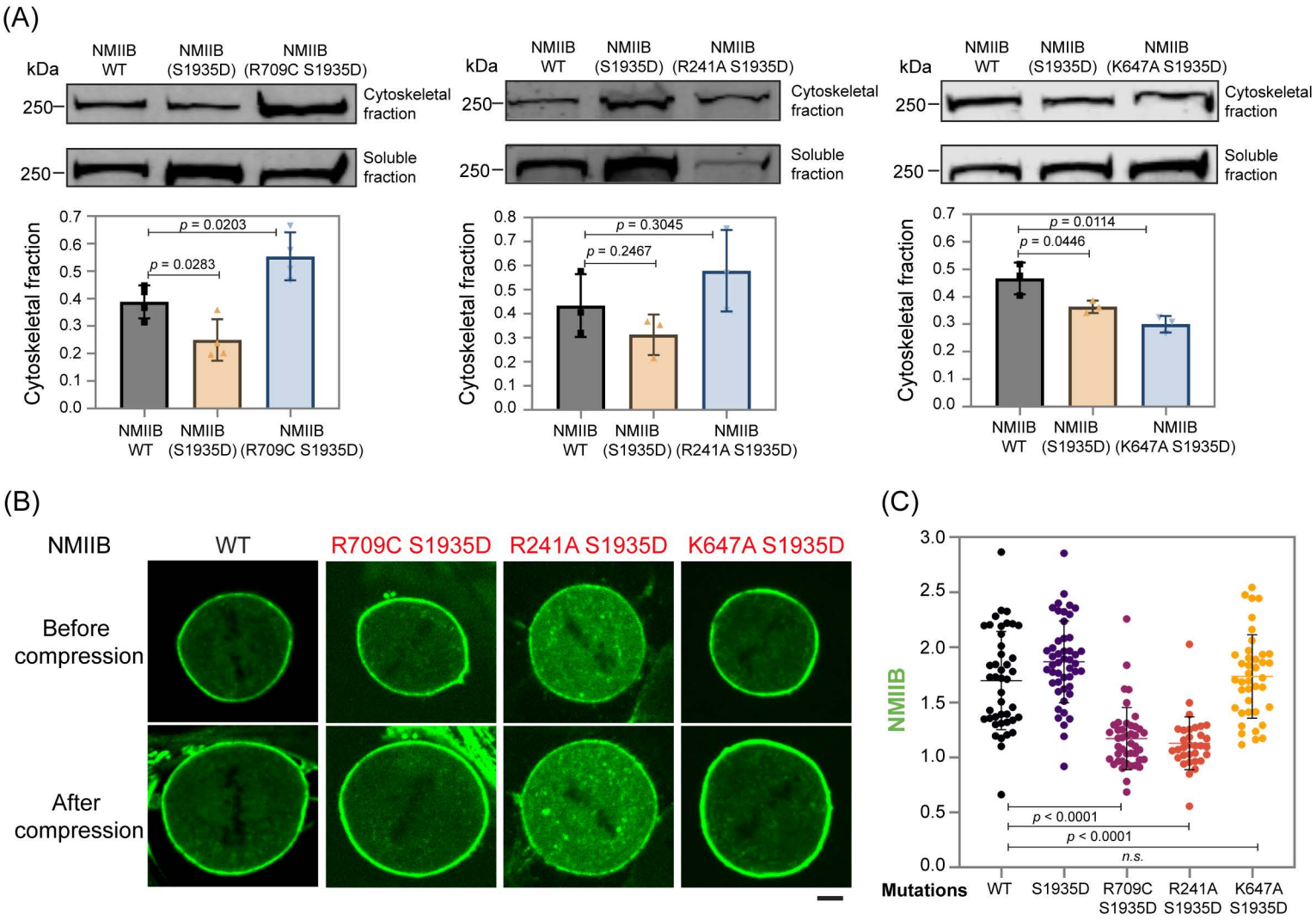
(A)
kDa
NMIIB WT
NMIIB (S1935D)
NMIIB (R709C S1935D)
250
Cytoskeletal fraction
Soluble fraction
Cytoskeletal fraction
p = 0.0203
p = 0.0283
NMIIB WT
NMIIB (S1935D)
NMIIB (R709C S1935D)
NMIIB (R241A S1935D)
p = 0.3045
p = 0.2467
NMIIB (K647A S1935D)
p = 0.0114
p = 0.0446
(B)
NMIIB
WT
R709C S1935D
R241A S1935D
K647A S1935D
Before compression
After compression
(C)
NMIIB
p < 0.0001
n.s.
Mutations
WT
S1935D
R709C S1935D
R241A S1935D
K647A S1935D

Figure S1

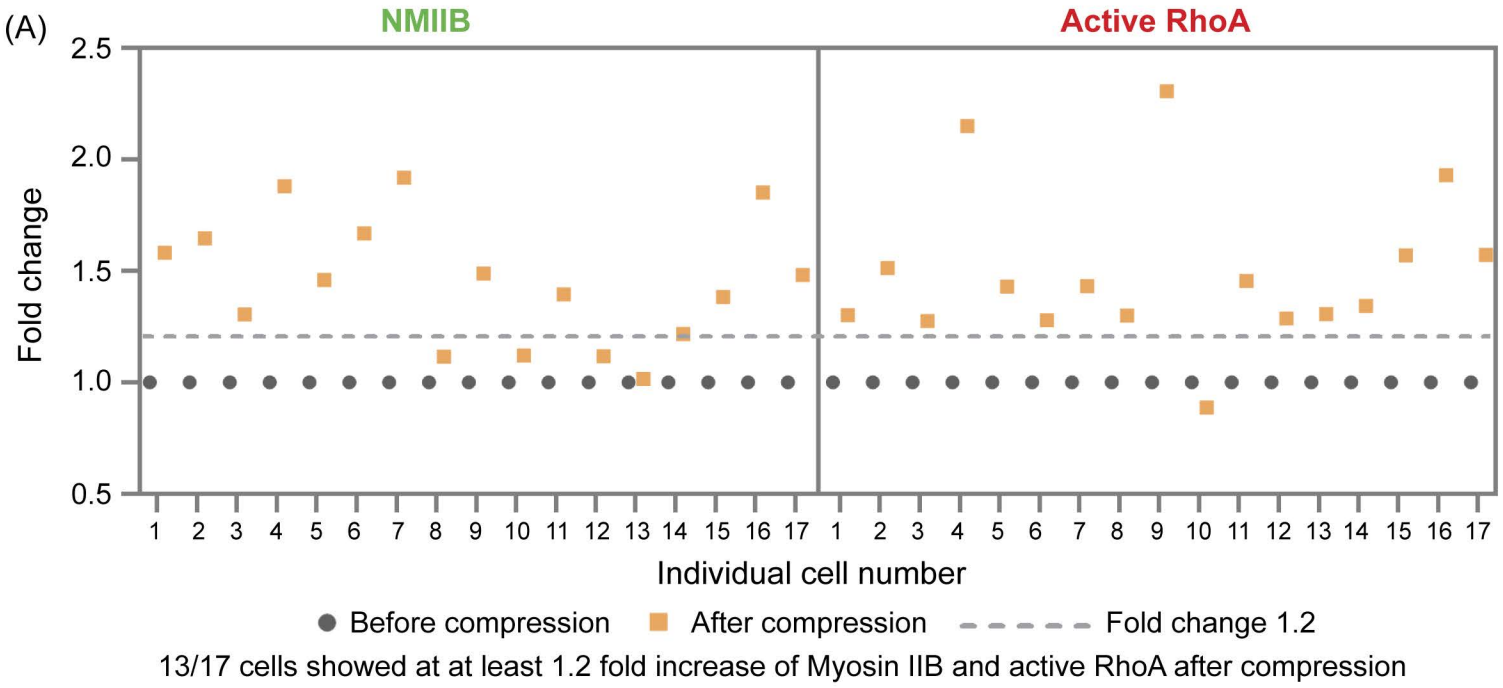

13/17 cells showed at at least 1.2 fold increase of Myosin IIB and active RhoA after compression

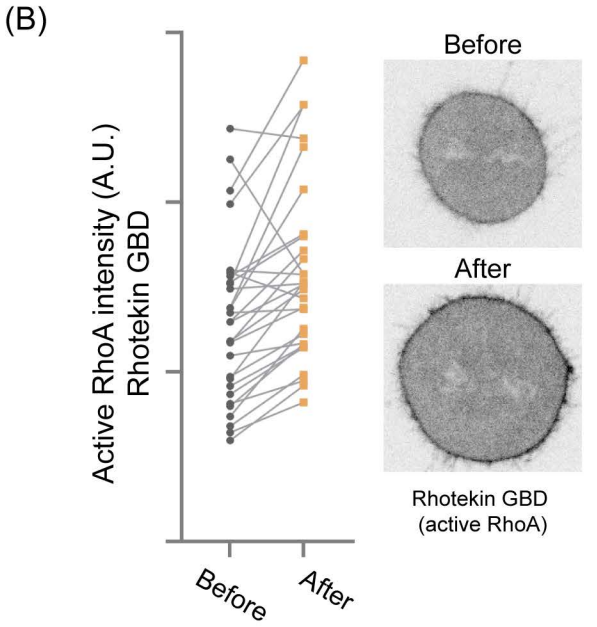

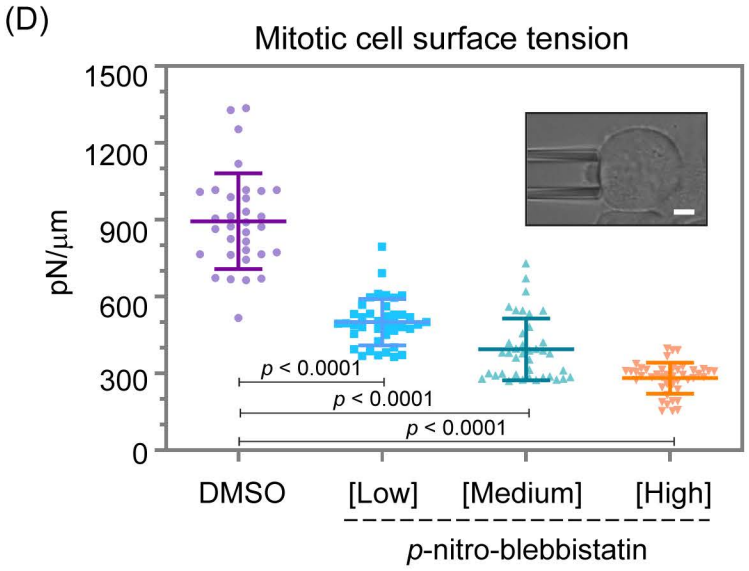

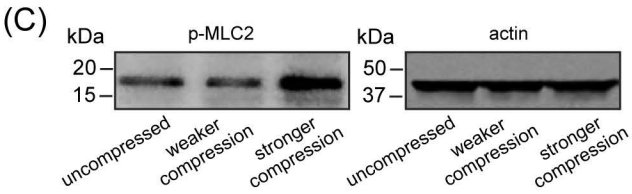

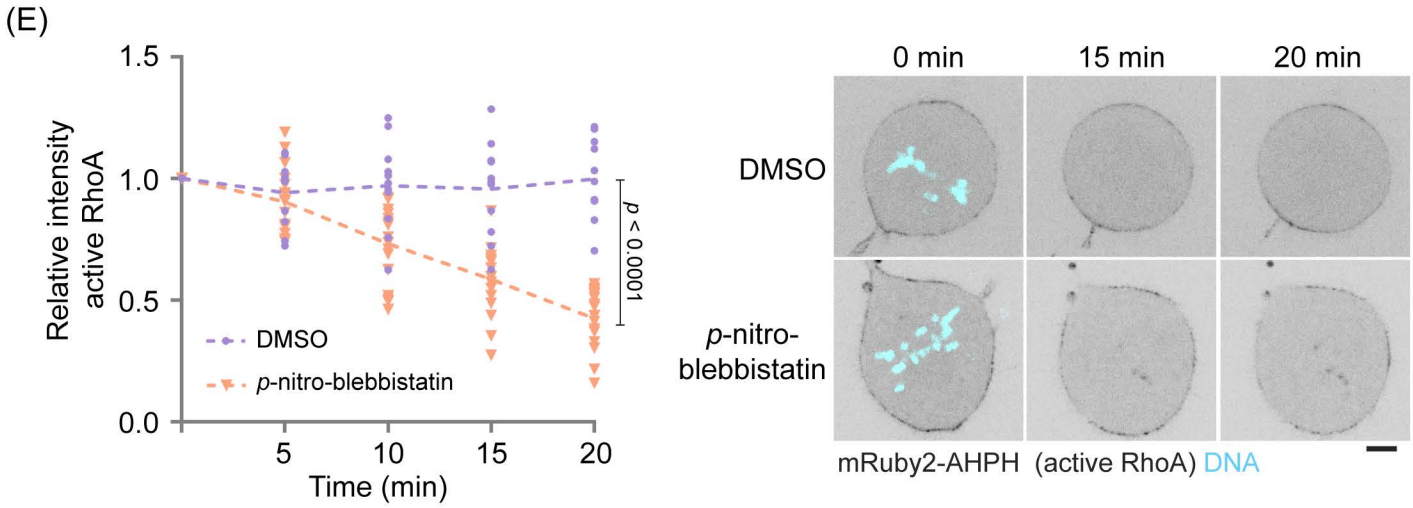

Figure S2

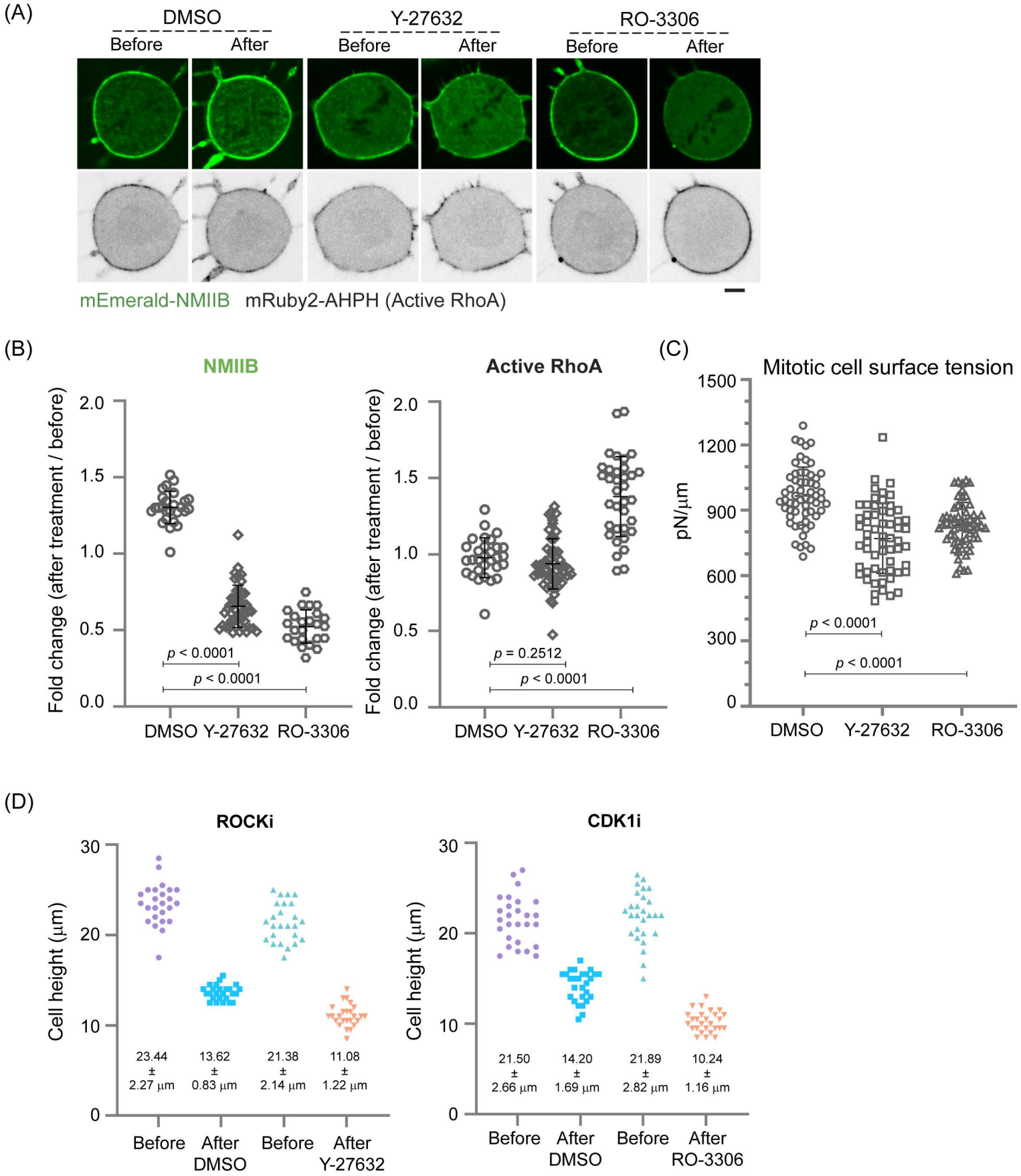
(A)
DMSO
Y-27632
RO-3306
Before
After
mEmerald-NMIIB
mRuby2-AHPH (Active RhoA)
(B)
NMIIB
Active RhoA
Fold change (after treatment / before)
2.0
1.5
1.0
0.5
0.0
p < 0.0001
p < 0.0001
p = 0.2512
DMSO
Y-27632
RO-3306
(C)
Mitotic cell surface tension
pN/μm
1500
1200
900
600
300
0
(D)
ROCKi
CDK1i
Cell height (μm)
30
20
10
0
23.44 ± 2.27 μm
13.62 ± 0.83 μm
21.38 ± 2.14 μm
11.08 ± 1.22 μm
21.50 ± 2.66 μm
14.20 ± 1.69 μm
21.89 ± 2.82 μm
10.24 ± 1.16 μm
Before
After DMSO
After Y-27632
After RO-3306

Figure S3

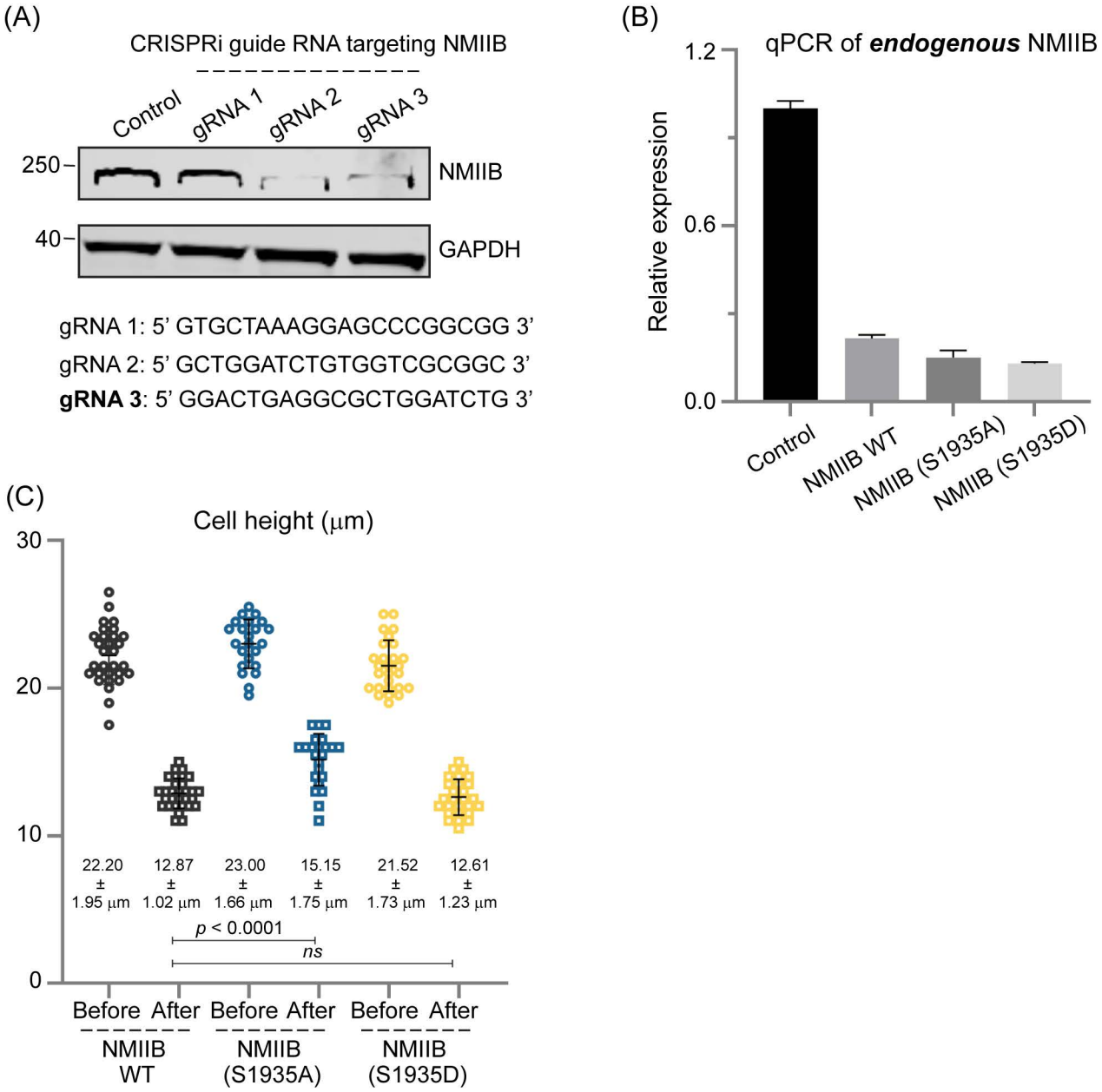
(A)
CRISPRi guide RNA targeting NMIIB
Control
gRNA 1
gRNA 2
gRNA 3
250
NMIIB
40
GAPDH
gRNA 1: 5' GTGCTAAAGGAGCCCGGCGG 3'
gRNA 2: 5' GCTGGATCTGTGGTCGCGGC 3'
gRNA 3: 5' GGACTGAGGCGCTGGATCTG 3'
(B)
qPCR of endogenous NMIIB
Relative expression
1.2
0.6
0.0
Control
NMIIB WT
NMIIB (S1935A)
NMIIB (S1935D)
(C)
Cell height (μm)
30
20
10
0
22.20 ± 1.95 μm
12.87 ± 1.02 μm
23.00 ± 1.66 μm
15.15 ± 1.75 μm
21.52 ± 1.73 μm
12.61 ± 1.23 μm
p < 0.0001
ns
Before
After
Before
After
Before
After
NMIIB WT
NMIIB (S1935A)
NMIIB (S1935D)